

A Comparison of Grid-Based and SPH Binary Mass-Transfer and Merger Simulations

Patrick M. Motl¹, Juhan Frank², Jan Staff³, Geoffrey C. Clayton², Christopher L. Fryer⁴, Wesley Even⁵, Steven Diehl^{4,5}, and Joel E. Tohline²

ABSTRACT

Currently there is great interest in the outcomes and astrophysical implications of mergers of double degenerate binaries. In a commonly adopted approximation, the components of such binaries are represented by polytropes with an index $n = 3/2$. We present detailed comparisons of stellar mass-transfer and merger simulations of polytropic binaries that have been carried out using two very different numerical algorithms — a finite-volume “grid” code and a smoothed-particle hydrodynamics (SPH) code. We find that there is agreement in both the ultimate outcomes of the evolutions and the intermediate stages if the initial conditions for each code are chosen to match as closely as possible. We find that even with closely matching initial setups, the time it takes to reach a concordant evolution differs between the two codes because the initial depth of contact cannot be matched exactly. There is a general tendency for SPH to yield higher mass transfer rates and faster evolution to the final outcome. We also present comparisons of simulations calculated from two different energy equations: in one series we assume a polytropic equation of state and in the other series an ideal gas equation of state. In the latter series of simulations an atmosphere forms around the accretor which can exchange angular momentum and cause a more rapid loss of orbital angular momentum. In the simulations presented here, the effect of the ideal equation of state is to de-stabilize the binary in both SPH and grid simulations, but the effect is more pronounced in the grid code.

Subject headings: binaries: close, hydrodynamics, methods: numerical, white dwarfs, AM CVn, Type Ia supernovae, R CrB

¹Indiana University Kokomo, School of Sciences, P.O. Box 9003, Kokomo, IN, 46903-9004, USA; pmotl@iuk.edu

²Louisiana State University, Department of Physics & Astronomy, 202 Nicholson Hall, Baton Rouge, LA 70803-4001, USA

³Department of Astronomy, University of Florida, Gainesville, FL, 32611, USA

⁴Computational Methods Group (CCS-2), Los Alamos National Laboratory, P.O. Box 1663, Los Alamos, NM, 87545, USA

⁵Theoretical Astrophysics Group (T-6)/Computational Methods Group (CCS-2), Los Alamos National Laboratory, P.O. Box 1663, Los Alamos, NM 87545, USA

1. Introduction

Dynamically unstable mass transfer and stellar mergers involve complex hydrodynamical flows of material through a varying gravitational potential. Investigating these rapid phases of stellar evolution requires the solution of Poisson’s equation (for the self-gravity of the binary) coupled to the equations of hydrodynamics to predict the outcome of the mass transfer event. The complexity of these coupled equations necessitate a numerical solution, of which several possible computational techniques are available – each with their own strengths, weaknesses and numerical artifacts.

In this paper we investigate mass transfer, tidal disruption and merger events in binaries using two very different numerical codes and we compare the results obtained. We follow the commonly adopted approximation in which the two stars are represented by $n = 3/2$ polytropes, and we limit our scope to cases where the stellar components are of comparable size. We are thus able to approximate, in some of our simulations, the scenario of two non-relativistic white dwarfs (WDs) in a binary when the less massive component first reaches contact with its Roche lobe. Even with this limitation such events are suspected to connect binary progenitors to a wide range of astrophysically interesting objects. This class of binary interactions and mergers is currently attracting considerable attention (see e.g. Staff et al. 2012; Pakmor et al. 2012; Dan et al. 2012, 2014; Pakmor et al. 2013, 2016; Zhu et al. 2013, and references therein). These efforts and others, in some cases using newly developed codes and novel techniques, also highlight the importance of benchmark runs to help establish the advantages and disadvantages of different codes. To help facilitate this process, the initial data for the runs presented in this paper are available to other groups interested in simulating interacting binary star systems through direct numerical simulations by contacting the corresponding author.

Recent observations and population synthesis models imply that there are a significant number of close double degenerate (DD) binaries in the Galaxy (Han 1998; Nelemans et al. 2005; Kilic et al. 2010, 2011; Parsons et al. 2011; Brown et al. 2011; Badenes & Maoz 2012). A majority of binaries, close enough to interact sometime during their evolution, will end up as DD systems where both stars are WDs (Nelemans et al. 2005; Badenes & Maoz 2012). The formation of such a close binary system will include two mass transfer phases, with at least one, more likely two, common envelope phases. If the resulting DD system has a short enough period ($\lesssim 0.2$ hr) it will enter a late phase of rapid mass-transfer and may merge in less than a Hubble time due to the loss of energy due to gravitational radiation (e.g. Postnov & Yungelson 2006, and references therein). This may result in a Type Ia supernova (SN) explosion if the total mass of the DD system is sufficiently large, or in a Type .Ia SNe explosion, a hot DQ white dwarf, sdO, R Coronae Borealis (RCB) or Hydrogen-Deficient Carbon (HdC) star if the mass is lower than this limit (Iben & Tutukov 1984; Webbink 1984; Yungelson et al. 1994). Longer-lived, interacting DD systems, such as AM CVn binaries, will produce gravitational radiation that should be detected by the evolved Laser Interferometer Space Antenna (eLISA), New Gravitational Wave Observatory (NGO) or their descendants (Amaro-Seoane et al. 2013).

Most of the simulations of WD mergers in the literature have been conducted using various versions of Smoothed Particle Hydrodynamics (SPH), with examples of recent contributions from the LANL group including (Raskin et al. 2009, 2010; Fryer et al. 2010; Raskin et al. 2012). In contrast, the LSU group is one of the few in the world using finite difference hydrodynamics (FDH) for this purpose (Motl et al. 2002; D’Souza et al. 2006 - henceforth DMTF06; Motl et al. 2007 - henceforth MFTD07; Staff et al. 2012). It has been known for a few years that the onset of mass transfer, the time the binary system lingers before entering the final phase of the merger or tidal disruption, and details of this final phase, are sensitive to initial conditions, the binary parameters, the equation of state assumed, the method used to drive the system to contact, and the choice of simulation technique (DMTF06, MFTD07, Dan et al. 2011, 2012). In particular, it is important to develop an understanding of the differences observed and documented in the literature between simulations conducted using SPH and those using FDH for nearly identical binary parameters. However, for this comparison to be meaningful, care must be taken to ensure that all the above referenced variables are controlled and chosen to be as close to identical as possible (see §2). In practice, however, small differences in the initial conditions could not be avoided because of the different way the fluid is represented in each method and technical limitations in the construction of initial models. The optimal way to achieve these goals is to put together a team with experts drawn from both camps and to design the comparison simulations to be concordant. Here we present the results of such a team effort.

We have conducted a suite of simulations of binary models with two independent codes based on very different numerical techniques. One code is based on an Eulerian formulation of the partial differential equations for fluid flow and the second employs the SPH technique which leverages the Lagrangian approach to computational fluid dynamics (See §2). To enable a detailed comparison of these simulations we have taken care to ensure that both codes (i) begin from the same equilibrium binaries as initial data, (ii) drive these binaries into contact in the same manner to attain a mass transfer rate that can be resolved numerically, and (iii) analyze the time series of data for simulations with both codes using the same diagnostic tools and visualization techniques.

In §2 we describe both our grid-based “Eulerian” code and SPH code in addition to detailing how we generate our initial data through the Self-Consistent Field (SCF) technique, formulate a particle distribution to match these grid-based models for SPH simulations as well as our choices for computing diagnostics from the simulations to compare. Then, in §3 we step through 23 different numerical evolutions performed with our two codes. We have used four different initial models that span the range of initial mass ratios where dynamical mass transfer instability and merger are possible. In addition to comparing the two numerical codes head-to-head, we vary numerical resolution, depth of contact and the assumed equation of state to better elucidate the differences between our two numerical techniques. Finally, in §4 we summarize our conclusions and highlight the elements that are common to both techniques for numerical simulations in addition to the distinctions we have identified as being likely the result of numerical artifacts arising in one formulation or the other.

2. Numerical Algorithms

From a computational science point of view, our separate groups have shared the goal of developing computational fluid dynamic (CFD) algorithms that can be used to accurately simulate binary mass-transfer events in a variety of astrophysical settings. We treat both stars as continuum fluid structures whose Newtonian gravitational fields and tidal interactions are modeled in a fully self-consistent fashion. We also employ numerical schemes that are designed to spatially resolve the interior structures of both stars as well as faithfully represent the complex, nonlinear dynamical flows that result from mass exchange between the two stars. The SPH technique serves as the foundation of the numerical code designed by the “LANL” group; the numerical code designed by the “LSU” group — hereafter, referred to as the “grid” code — employs an Eulerian grid and uses a finite-volume discretization technique. The distinguishing attributes of both codes are described in §2.2, below. Here we briefly summarize key elements that are common to both codes.

Using explicit techniques, we integrate forward in time the set of partial differential equations (PDEs) that govern inviscid, compressible fluid flows. These include the continuity equation governing mass conservation, a vector equation of motion governing conservation of the three components of momentum, and an energy conservation equation. Only two physical source terms explicitly appear in the equation of motion: an acceleration due to gravity and an acceleration arising from local gradients in the gas pressure. In the context of the simulations being conducted here, principally for comparison purposes, we adopt one of two algebraic equations of state (EOS). For “polytropic” simulations, gas pressure P is derived from the mass density ρ via the relation,

$$P = \kappa_i \rho^\gamma, \quad (1)$$

where the adopted adiabatic exponent is $\gamma = \frac{5}{3}$ and the polytropic constant κ_i , which specifies the specific entropy of a fluid element, can have one of two values depending on whether the fluid element is originally part of the donor star ($i = D$) or part of the accretor ($i = A$). (Values of κ_A and κ_D , are reported in Table 1 for the initial models considered here.) For “ideal gas” simulations, we use the relation,

$$P = (\gamma - 1)\epsilon\rho, \quad (2)$$

where $\gamma = \frac{5}{3}$ and where, at each integration time step, the specific internal energy of the gas, ϵ , is determined from the PDE that governs energy conservation. As noted in Table 1, this equation of state allows us to simulate low mass (compared to the Chandrasekhar mass) double white binaries when both binary components are on the same adiabat. In other cases, the binary components will have the mass – radius relation appropriate to low-mass, fully convective stars.

Both codes employ mechanisms for handling the formation and movement of shock discontinuities. Via the energy equation, for example, some kinetic energy is converted to heat when the fluid passes through a shock. Hence, the specific entropy of a fluid element should also increase when the fluid passes through a shock. In practice, this additional heat will be realized by an increase in ϵ that is above what would be expected through adiabatic compression alone. When the ideal gas

EOS is used, the gas pressure also will reflect this heat gain because, via Eq. (2), P is proportional to ϵ . However, when the polytropic EOS is used, this additional heat is effectively lost from the system because the specific entropy of each fluid element is forced to remain constant, independent of whether or not the fluid has passed through a shock. By evolving otherwise identical systems, first, with a polytropic (P) EOS then, second, with an ideal gas (I) EOS, the set of simulations presented here not only permits us to compare results from different algorithmic techniques but also to isolate the effects that shock heating has on binary mass-transfer evolutions.

Results from CFD simulations can depend sensitively on initial conditions. With this in mind, we have made a concerted effort to start each simulation from a well-defined, equilibrium binary configuration, and to start each pair of comparison simulations from initial configurations that are nearly identical. The initial binary configuration for each of the 23 simulations identified in Table 2 was drawn from one of the equilibrium configurations listed in Table 1. By design, the models span a range of initial binary mass ratios, $1.323 \geq q_0 = M_D/M_A \geq 0.4085$ that includes the regime where mass transfer is dynamically unstable ($q_0 > q_{\text{crit}}$) to smaller initial mass ratios where mass transfer may be stable depending on the fate of the angular momentum of the accretion stream. For our chosen polytropic exponent of $\gamma = \frac{5}{3}$, the standard critical mass ratio for dynamical stability is $q_{\text{crit}} = \frac{2}{3}$ (Rappaport et al. 1982; Soberman et al. 1997), but could be significantly lower for direct impact accretion (e.g. $q_{\text{crit}} = 0.22$ Marsh et al. 2004; Gokhale et al. 2007). Table 1 includes the radii of each binary component as well as the accretor’s radii in units of the circularization radius, R_{circ} (where R_{circ} is calculated from equation 4.20 of Frank et al. 2002), showing that all of our initial models will experience direct impact accretion.

The initial models identified in Table 1 as Q1.3, Q0.5, and Q0.4a were selected for this investigation because their polytropic simulations had already been studied using the grid code (see DMTF06 and MFTD07). In each of these cases the detailed structure of the initial equilibrium configuration was derived using an SCF technique as described in §2.1.1, below. In the context of our present investigation, these three initial model configurations were each mapped to a particle distribution as described in §2.1.2 that was suitable for insertion as an initial model into the SPH code. We decided that we should also study the evolution of a binary system with an initial mass ratio $q_0 = 0.7$ because this was near the analytically predicted critical value, $q_{\text{crit}} = 2/3$, and filled a gap in parameter values that would otherwise exist between models Q1.3 and Q0.5. The standard SCF technique was used to construct the model identified as Q0.7a in Table 1 as the additional initial model for the grid code. But, in this case, a separate relaxation technique was used to generate the model identified in Table 1 as Q0.7b for insertion into the SPH code (See §2.1.2). We note that models Q0.7a and Q0.7b are very similar but not identical to one another; for example $\kappa_A \neq \kappa_D$ in Q0.7a. An additional SCF model, Q0.4b, at higher numerical resolution, was also constructed. As detailed in Table 1, the polytropic models Q0.4a and Q0.4b differ slightly in their parameters due to the difference in numerical resolution used for the SCF code.

As constructed, the donor star did not quite fill its Roche lobe in each initial model. After introducing an initial model into one of the two CFD codes, we “drove” the donor into contact

with its Roche lobe by explicitly extracting angular momentum from the binary system at rate of one percent per orbit for a specified “driving duration.” (The precise manner by which angular momentum was extracted from the binary system in the two separate CFD codes is described in §2.2.) Column 5 in Table 2 lists the driving duration that was chosen for each simulation.

2.1. Initial Conditions Setup

2.1.1. The Self-Consistent Field Method (SCF)

We use the SCF technique developed by Hachisu (Hachisu 1986; Hachisu et al. 1986) to generate our initial models. This approach allows us to form semi-detached equilibrium structures for the binary components that are synchronously rotating assuming a polytropic equation of state. These equilibrium structures naturally incorporate the effects of tidal distortion in their self-consistent Roche geometry as well as rotational flattening of the stars.

In a frame of reference co-rotating with the binary, the fluid equations reduce to a single scalar equation for each binary component that equates the sum of the gravitational potential, centrifugal potential and enthalpy to an integration constant. Three boundary points are set along the line of centers where the mass density is forced to vanish and these boundary points allow us to algebraically solve for the integration constant for each star and the angular frequency of the rotating frame.

We iteratively solve the scalar equations starting from spherical Gaussian density distributions and the Keplerian estimate for the orbital frequency. Upon solving Poisson’s equation (on a cylindrical mesh identical to the one used in the grid-based CFD code) we have an estimate of the enthalpy field. For our chosen polytropic equation of state, the enthalpy determines the next guess at the matter density where we rescale the density to maintain prescribed maximum density values for each star and an improved estimate of the centrifugal potential is computed about the current center of mass of the binary. Poisson’s equation is solved again and new values for the integration constants and orbital frequency are computed from the boundary conditions.

The iteration proceeds until the structure changes by an amount smaller than a given tolerance in each subsequent iteration. The converged value of the orbital frequency, Ω_0 , is used to initialize the velocity field in our binary simulations and to define the angular frequency of the grid code’s rotating frame of reference. The equilibrium solution is not exact however and the orbit will not be precisely circular but rather exhibit epicyclic oscillations about the mean binary separation even if artificial driving is not imposed. For the models constructed in this paper, the amplitude of $\frac{\dot{a}}{a}$, where time is measured in the initial orbital period of the binary, ranges from ~ 0.02 to almost 0.1 at the end of the driving phase. We note as well that, throughout this paper, $P_0 \equiv 2\pi/\Omega_0$, as quantified in Table 1, is used to normalize evolutionary times. In the grid-based simulations, the converged SCF model is shifted slightly within the grid, via an interpolation scheme, before it

is introduced into the CFD code in order to better ensure that the center of mass of the binary system initially coincides with the origin of the cylindrical coordinate system.

2.1.2. Application to SPH Initial Conditions

For SPH simulations, the particle distribution has to be chosen *a priori*. Since we want to pay particular attention to resolving the Roche lobe overflow accretion stream, we need sufficient resolution (i.e. particles) in the outer layers of the donor. Since the SCF method yields asymmetric stellar configurations, we developed a new setup technique for SPH initial conditions that can handle arbitrary spatial configurations. This technique is based on weighted Voronoi tessellation (WVT) and is discussed in greater detail in Diehl et al. (2012). For the sake of completeness, we here discuss the essentials as well as details specific to the SCF setup problem.

The WVT initial condition setup is based on an approach developed by Diehl & Statler (2006) to adaptively bin two-dimensional astronomical X-ray images to a constant signal-to-noise ratio. We extend this technique to work in arbitrary dimensions, and optimize the algorithm to work with an underlying, arbitrary probability distribution instead of images. The algorithm starts out with an initial guess for the particle distribution, which we choose to be random positions drawn from the probability distribution. The WVT setup then iteratively applies artificial short-range (typically within 2-3 smoothing lengths) forces to the particles until they settle into a smooth particle distribution. The strengths of these forces are determined by the desired input resolution at the particle positions. This process generally converges rather quickly (< 40 iterations) and results in a setup with very low particle-noise, and the desired particle distribution. For uniform distributions, the configuration resembles that of gravitational glasses, which are often employed in cosmological simulations (e.g. Diehl et al. 2012; Wang & White 2007).

In the context of this investigation, we apply a uniform particle distribution for the accretor. In a high-resolution SPH simulation, each accretor is modeled with a total of 150,000 SPH particles. In order to properly resolve the accretion stream and beat down the noise in the mass transfer rate due to a small number of SPH particles, we decided to resolve the outer layers of the donor star with much higher precision. The resolution at the center of the donor star is chosen to match approximately that of the accretor. However, the smoothing lengths in the outer layers are approximately 4 times smaller, putting effectively ~ 64 more resolution elements in these layers, adding up to a total of 850,000 SPH particles in the donor star and, hence, approximately 1,000,000 particles for each full simulation. Figure 1 shows a slice through the meridional plane of the WVT SPH setup for initial model Q0.4a, as defined in Table 1. For clarity, only particles within one smoothing length of the meridional plane are plotted.

The SPH density interpolation of the particle masses in the WVT method generally reproduces the SCF grid setup to better than 1%, as shown in Figure 2 where we show mass profiles for the stellar components in the initial states. Despite the fact that the stars are not spherically

symmetric, we construct the mass profile as the mass within spherical shells centered on the center of mass of each stellar component. Integral quantities for the initial states including the total angular momentum, orbital angular momentum and the spin angular momentum of each binary component agree to a level of 1% or better for models Q0.4a, Q0.5 and Q1.3. For model Q0.7b, a separate, simpler relaxation method was used starting with two perfect spheres placed at the expected orbital separation. Centrifugal and tidal distortions were then introduced adiabatically allowing the components to relax to equilibrium.

2.2. Computational Fluid Dynamic Techniques

2.2.1. Finite-volume “grid” code

Our finite-volume “grid” code is an explicit code that is second order accurate in both time and space and has been used extensively to simulate self-gravitating astrophysical flows (Motl et al. 2002; D’Souza et al. 2006; Motl et al. 2007; Staff et al. 2012). The code utilizes cylindrical coordinates and evolves equations for the conservation of mass, radial, vertical, and angular momentum and an energy equation, as described in more detail below. With our choice of coordinates and formulation of the fluid equations we are guaranteed that the total angular momentum of the system will not change due to advection or due to gravitational or pressure forces.

The hydrodynamics treatment is similar to that in the Zeus code (Stone & Norman 1992); we use advection operators based on Van Leer slopes and a similar numerical viscosity to stabilize the fluid equations in the presence of shocks. The fluid equations are formulated for a rotating reference frame (including source terms for the associated Coriolis and centrifugal forces) and we set the code’s reference frame to rotate at the initial orbital frequency of the binary to minimize the effects of numerical diffusion through the grid. Further details of the hydrodynamics algorithm are available in Motl et al. (2002) and D’Souza et al. (2006).

For polytropic simulations our energy equation is cast in terms of an entropy tracer

$$\tau = (\epsilon\rho)^{1/\gamma} \quad (3)$$

where ϵ is the specific internal energy of the fluid and ρ is the mass density. The entropy tracer evolves with an advection equation similar to the continuity equation for polytropic simulations. For simulations with an ideal gas equation of state we evolve the total energy density, E , with

$$\frac{\partial E}{\partial t} + \nabla \cdot \mathbf{v}E = -\nabla \cdot p\mathbf{v} - \rho\mathbf{v} \cdot \nabla\Phi_{\text{eff}} \quad (4)$$

where Φ_{eff} includes both the gravitational and centrifugal potentials. We compute the internal energy of the fluid by subtracting the kinetic energy density of the fluid from the total energy density.

The fluid equations evolve densities of conserved quantities like mass density or momentum density but updating the fluid state requires additional quantities that don’t obey conservation

laws like the velocity of the fluid. We are thus continually dividing by the mass density of the fluid and therefore no cell in the grid can have a vanishing mass density. To prevent division by zero, we floor the mass density at every timestep and for the runs presented here the floor density is $\rho_{\min} = 1 \times 10^{-10}$ compared to a maximum stellar density of ~ 1 and a characteristic density at the stellar edge of approximately 10^{-5} . The entropy tracer, τ , is floored similarly to ρ in polytropic evolutions to remain above a value

$$\tau_{\min} = \left(\frac{\kappa_{\min}}{\gamma - 1} \right)^{\frac{1}{\gamma}} \rho_{\min} \quad (5)$$

where κ_{\min} is the smaller of the polytropic constants in the binary system. For simulations with an ideal gas equation of state, the total energy density E is floored to remain above the smallest internal energy density, τ_{\min}^{γ} .

Poisson’s equation is solved by performing a Fourier analysis along the periodic azimuthal direction and an alternating-direction implicit technique is used for the radial and vertical directions. The boundary value of the gravitational potential is computed via a numerical integration of the mass density with cylindrical Greens functions based on half-integer degree Legendre polynomials of the second kind (Cohl & Tohline 1999; Cohl et al. 2001). We employ outflow boundary conditions at the outer edge of the computational domain and over the course of a merger simulation, up to $\sim 0.3\%$ of a system’s total mass can be lost from the active grid.

As was alluded to above, each binary simulation was begun with a phase of artificial “driving” that causes the orbit to slowly decay and forces the donor star into contact with its Roche lobe. This establishes a mass transfer stream that can be well resolved by the code, given the chosen numerical resolution. In the grid code the phase of driving was accomplished by removing a fraction of the specific angular momentum of each fluid element each time step of the simulation at a rate such that one percent of the initial angular momentum is removed per initial orbital period, P_0 .

A typical numerical simulation with the grid code (at a numerical resolution of 162 radial zones by 98 vertical zones by 256 azimuthal zones for a total of approximately 4 million cells as listed in Table 2) required about 24 days of run time on 64 cores of the Louisiana Optical Network Initiative (LONI) machine QueenBee, assuming a polytropic equation of state. With the ideal gas equation of state, the sound speed is higher which further reduces the Courant-Friedrichs-Lewy (CFL) limited time step and increases the typical run time to approximately 150 days. The higher sound speed for ideal gas equation of state simulations results from a hot, low density envelope of shock heated material that forms around the accreting star. Note that, since we are using a cylindrical coordinate grid, the CFL limiting constraint on the time step is often reached near the coordinate axis and is thus significantly smaller than would be the case with a Cartesian coordinate grid.

2.2.2. *Smooth Particle Hydrodynamics (SPH) code*

The SPH code used in this work is called SNSPH, and is described in much greater detail in Fryer et al. (2006). Here we will give a global overview of the code, focusing on the aspects most important to this project.

SNSPH is a tree-based, massively parallel SPH code that has undergone rigorous testing and has been applied to a large variety of astrophysical problems (e.g. Fryer & Warren 2002; Young et al. 2006; Diehl et al. 2008). The gravitational forces are evaluated in an order $N \log N$ gravitational tree, where long-range forces are replaced by monopole terms. Our multipole acceptance criterion is described in Warren & Salmon (1995) and is designed to provide a direct bound on the error budget associated with the monopole approximation.

There are several flavors of SNSPH, and each integrates the hydrodynamics equations in a slightly different manner. For this investigation we have chosen the version that integrates the specific internal energy in order to facilitate a direct determination of temperatures from the SPH simulations. For our SNSPH calculations, we use the simple viscosity prescription utilizing both bulk (α) and von Neumann-Richtmyer (β) viscosity coefficients (Benz 1990; Monaghan 1992, 2005; Fryer et al. 2006). We do not evolve these constants, and most of our calculations used standard values: $\alpha = 0.5$, $\beta = 2.0$. However, we did run a test calculation using $\alpha = 0.125$ and $\beta = 0.5$ and our answers did not change noticeably.

For this work, we have included several improvements of the SNSPH code. First, the traditional n-body Plummer softening of the gravitational acceleration of the SPH particles has been replaced with an SPH-kernel based smoothing (see Benz 1990; Nelson 2006, for example), where the SPH kernel is interpreted as a three-dimensional density distribution, and the gravity is calculated self-consistently according to this distribution. The main advantage of this spatially adaptive, but computationally slightly more intensive prescription is that the gravitational acceleration between two particles vanishes as they come very close to each other. This in turn reduces the frequency of an SPH-specific numerical artifact, known as “particle-pairing” or the “pairing instability” (e.g. Thomas & Couchman 1992; Herant 1994; Nelson 2006), which can drastically reduce the effective resolution of an SPH simulation. In a sense, the binary simulations conducted here with a polytropic equation of state present a worst-case scenario for the particle-pairing problem. In the Q0.4P simulations (see the last row of Table 1), for example, the donor material that streams onto the surface of the accretor has a lower specific entropy than the original accretor material, meaning that the donor material is convectively unstable and some high-resolution donor particles sink deep into the accretor. In the process, the already small, low-density donor particles get even further compressed and clump to each other, forcing the particles to become extremely close.

To further reduce particle-pairing and to avoid code-specific numerical problems in the tree setup, we also introduce a repulsive pressure wall within the innermost 2% of the particle smoothing length (see Thomas & Couchman 1992, for a similar approach). Due to the small volume affected by this modified artificial pressure force, this choice does not affect the overall performance and

conservational properties of the code.

As with the grid-based evolutions, the SPH components were driven into contact by removing angular momentum from the binary at a prescribed rate for a specified duration. This was accomplished in the SPH simulations by reducing the velocity of the SPH particles through a user-specified time derivative of the angular velocity.

The 1 million particle SPH simulations in this paper generally ran on 128 processors for about one week clock time on the AMD Opteron cluster *Coyote* located at Los Alamos National Laboratory.

2.3. Diagnostics

Our analysis of each binary simulation has been carried out primarily using two diagnostic techniques: (1) Throughout each simulation, a variety of global binary parameters were evaluated by performing integrals over the computational volume as detailed in Appendix A, and then curves were plotted to show the variation with time of these parameters. (2) For each simulation, a movie was generated to show the time-variation of the matter distribution. We determined the degree to which a simulation performed with the SPH code resembled the simulation performed with the grid code by comparing the behavior of various parameter curves and/or by comparing corresponding frames from movies generated with the two separate codes.

Most of the figures shown in subsequent sections of this paper display results from either one or both of these diagnostics. For example, the curves drawn in Figure 3a show the time-dependent behavior of six binary system parameters derived from three separate Q1.3P simulations — orbital separation, a , binary mass ratio, q , log of the donor’s mass-transfer rate, $|\dot{M}_D|$, orbital angular momentum, J_{orb} , and spin angular momentum of the accretor, J_A , and donor, J_D . The color contour plots shown in Figure 3b are movie frames drawn from two separate points in time during two of these Q1.3P simulations. Since the two numerical codes use different frames of reference, an inertial reference frame in the case of the SPH simulations and a frame of reference rotating at the initial frequency of the binary in the grid simulations, there will be a trivial phase angle offset between the two codes. For the purpose of aiding comparisons between the two codes, the grid code data are rotated to match the phase of the SPH simulation for the color contour plots of the projected mass density. Throughout the paper, such figures are used to illustrate key findings from our comparison simulations. We also note that, in general, the frames taken from our grid code simulations show an outline of the outer edge of the cylindrical grid at low density levels. This is a numerical artifact resulting from imperfect outflow boundary conditions applied at the outer edge of the computational domain.

Initially we agreed that the group that developed the SPH code and the group that developed the grid code would perform these diagnostic analyses independently. Eventually we realized that some differences that appeared when comparing diagnostics from different simulations arose from

subtle differences that appeared in the volume integrals that were being used by the two different groups to define various global binary parameters. There are, for example, different ways to define the orbital angular momentum or the spins of the two stars when some of the matter resides in an envelope that is shared by the two stars. We ultimately decided, for diagnostic purposes only, to map results from the SPH simulation onto a 3D grid and to use the diagnostic software developed for the grid code to also analyze results from each SPH simulation. The diagnostic figures presented throughout the remaining sections of this paper were derived in this manner. Appendix A explains how each volume integral was defined in order to evaluate the various global binary parameters.

The initial data for the Q0.7 binary were developed independently by the two groups resulting in the models Q0.7a and Q0.7b described in Table 1. We made use of the freedom of the chosen polytropic equation of state to re-scale the data from the grid evolutions to match the total mass and initial separation of the SPH model Q0.7b for the purposes of analyzing the simulation results. Both the line plots and images of the projected mass density from the grid code have been rescaled accordingly.

3. Evolutions

As is cataloged in Table 3, we are reporting on results from 23 separate binary mass-transfer simulations. Each of the simulations was followed through at least eight, usually more than a dozen, and up to fifty orbits with each individual orbit requiring tens of thousands of Courant-limited integration time steps (for the grid code simulations). Hence, our critical examination of the behavior of these systems and, most importantly, the comparison of behavior between different simulations, has required the analysis of a tremendous amount of simulation data. In what follows, our formal discussion of the results is broken down into a series of subsections that, generally speaking, march through the models in the order in which they are listed in Table 2.

Before diving into the details, the reader may find it advantageous to skim through the figures and/or some of the accompanying movies (21 in total, as labeled in column 5 of Table 3) in order to sample the variety of physical phenomena that arise in these types of systems. Examples are:

- Binary merger – see video01 or video02, and Figure 3b;
- Tidal disruption of the donor – see video04, video16, or video21, and Figure 4b or Figure 14;
- The hot, tenuous common envelope that forms in “ideal gas,” as opposed to “polytropic,” simulations – compare video07 to video17, and see Figure 9;
- Nonaxisymmetric modes having four-sided (box-like) and three-sided (triangular) shapes excited in an accretion disk – see video07 or video12, and Figure 8;
- Binary detachment following a long phase of relatively stable mass transfer – see video07, video09, or video11.

3.1. Polytropic Simulations

Here we discuss and compare results from simulations that were carried out using a polytropic equation of state. The relevant simulations are labeled as Q1.3P, Q0.7P, Q0.5P, and Q0.4P along with a two-character model identification suffix (for example, simulation Q1.3P_G1) in the first 13 rows of Table 2. In each case the structure of the binary system at time $t = 0$ was prescribed by one of the five, initially uniformly rotating, $n = \frac{3}{2}$ polytropic binary models identified in Table 1. At the start of a simulation, the donor star was driven into contact with its Roche lobe by artificially draining angular momentum from the system at a rate of one percent per orbit for the “driving duration” specified in column 5 of Table 2. Thereafter the system was evolved in a fully self-consistent fashion without further external influences. As is documented in column 4 of Table 2, some SPH simulations were carried out using 100 thousand ($100k$) particles and others used 1 million ($1M$) particles; most simulations performed with the grid code used a uniform cylindrical grid containing approximately four million grid cells but we include one grid simulation of the Q0.4P system at a higher resolution of approximately 47 million ($47M$) cells.

To aid in our analysis, we have established the time of an event common to each merger simulation, the merger time, t_{merge} , as a means of synchronizing these simulations. While the choice of the exact merger time is in some sense arbitrary, we have found empirically that the first data set where the merged object has only one density concentration could be identified relatively easily by eye. We found this particular choice of merger time could be identified in a repeatable manner for both grid and SPH data sets from the animations corresponding to each simulation. Merger times are recorded in the third column of Table 3 for those simulations that merge. With a common event identified in all merger simulations, we can measure time relative to t_{merge} to eliminate trivial phase differences and variations in instability growth rates in different simulations to compare the highly nonlinear state of the evolving fluid in a clear way. From t_{merge} we have established a zero point time relative to a particular grid-based simulation as,

$$(t_{\text{zpt}})_{\text{ID}} = (t_{\text{merge}})_{\text{G1}} - (t_{\text{merge}})_{\text{ID}}. \quad (6)$$

Time sequences of data from a particular simulation can be compared then by plotting the behavior of various system parameters using the *shifted* time,

$$t_{\text{shift}} \equiv t + t_{\text{zpt}}, \quad (7)$$

to label the temporal axis. For reference, column 4 of Table 3 contains t_{zpt} for each merger simulation.

3.1.1. Q1.3P Model Simulations

We carried out three separate adiabatic simulations of the binary polytrope that had an initial mass ratio $q_0 = 1.323$. In each case, in order to initiate mass transfer, the model was driven at a

rate of 1% per orbit for $2.0P_0$. As is indicated by the note referenced in the last column of Table 2, some results from the grid-code simulation Q1.3P_G1 already have been presented as simulation Q1.3-D in §5.1.1 of DMTF06. This model, as shown in Table 1, has an equation of state appropriate for fully convective, and hence low mass, main sequence stars and in this case it is the larger, more massive star that has reached contact with its Roche lobe.

Whether the simulation was conducted using the grid code (model *G1*) or the SPH code (models *S1* and *S2*), the Q1.3P simulation was found to be dynamically unstable to mass transfer. This was as expected theoretically because the system had an initial mass ratio greater than unity and, therefore, also greater than q_{crit} . As Figure 3a illustrates, throughout each model simulation, the binary separation (a) and system mass-ratio (q) steadily decreased while the donor mass-transfer rate ($|\dot{M}_D|$) steadily increased. As is shown in the accompanying movies – video01 from simulation Q1.3P_G1, video02 from simulation Q1.3P_S1, and video03 from simulation Q1.3P_S2 – and as is illustrated by the images shown in Figure 3b, independent of the chosen numerical technique the two stars ultimately merged violently in the sense that the highest density “core” region of the donor was observed to collide and combine with the highest density “core” region of the accretor.

The upper right-hand image shown in Figure 3b is the frame picked from the movie of grid-code simulation Q1.3P_G1 at the instant the cores of the two stars first merge, that is, at the instant the donor core is no longer distinguishable from the core of the accretor. Defined in this way, the merger time for simulation Q1.3P_G1 is $t_{\text{merge}} = 12.38P_0$. The lower right-hand image in Figure 3b is the frame picked from the movie of SPH-code simulation Q1.3P_S1 that most closely resembles the upper right-hand image. Using this frame to define the instant of merger, we deduce $t_{\text{merge}} = 7.57P_0$ for simulation Q1.3P_S1. In a similar manner we have deduced that $t_{\text{merge}} = 8.17P_0$ for the lower resolution SPH-code simulation Q1.3P_S2.

The “instant of merger” frames selected from simulations Q1.3P_G1 and Q1.3P_S1 are not just similar qualitatively, they share a considerable amount of detail. In both cases the merged core displays a marked top/bottom asymmetry: the bottom edge of the core is flat, revealing the shock front that was established by the core collision; the top is elongated largely by donor material, giving the merged core the shape of an egg. Toward the bottom, the small, remnant tail of the donor that has not yet plunged through the shock has the same structure in both models. Furthermore, the models display remarkably similar details where the trailing edges of both spiral arms branch at sharp angles from the merged core.

The left-hand images in Figure 3b present frames from both movies one quarter of an orbit prior to merger — the top frame is drawn from the movie of grid-code simulation Q1.3P_G1 and the bottom frame is drawn from the movie of SPH-code simulation Q1.3P_S1. These two images also display a high degree of quantitative similarity. They illustrate what a careful viewing of video01, video02, and video03 reveals: the two different numerical schemes produce very similar dynamical results, especially as the simulations each evolve through the time of merger. Note that the SPH simulations are conducted in an inertial frame whereas the grid-code simulations are computed in

a frame initially corotating with the binary. Consequently, in all the figures showing comparisons of equatorial density distributions obtained with both codes, we have rotated the density contours obtained with the grid code to match the orientation of those obtained with the SPH code.

We cannot ignore the fact that the precise time of merger was different in the three simulations. The decidedly different merger times seem to suggest that different code algorithms or model resolutions produce different results. But a more careful examination reveals that if an appropriate zero-point time-shift, t_{zpt} , is added to the recorded evolutionary time of each simulation, the simulations show a high degree of agreement. For this particular set of models, the merger times have been used to define t_{zpt} as shown in column 4 of Table 3. In Figure 3a the time-evolutionary behavior of various system parameters has been displayed using the shifted time that synchronizes merger between the simulations. Viewed from this perspective, we conclude again that the three separate Q1.3P simulations show a remarkable level of agreement.

Consider first the middle panel on the right-hand-side of Figure 3a, which displays the time-dependent behavior of the system’s orbital angular momentum. During the first two orbits, J_{orb} steadily decreases at a rate of 1% per orbit due to the imposed driving, then it remains nearly constant until the merger occurs. Over the last ~ 6 orbits, the (solid blue) curve generated by the 1M-particle SPH simulation lies directly on top of the (solid red) curve drawn from the 4M-cell grid-code simulation. The slight mismatch exhibited by the (dashed blue) curve drawn from the lower resolution (100 K) SPH simulation simply reflects the inability of the lower-resolution model to accurately represent the system’s initial J_{orb} . After the zero-point shift in time has been taken into account, all three curves that describe the time-evolutionary behavior of the binary separation (see the top panel on the left-hand side of Figure 3a) also lie on top of one another over the last $\sim 6P_0$.

All three simulations show that, once mass-transfer commences, the rate increases by more than two orders of magnitude in less than 10 orbits; see the middle panel on the left-hand side of Figure 3a. It is gratifying to see that, after t_{zpt} has been taken into account, all three $|\dot{M}_{\text{D}}|$ diagnostic curves converge immediately prior to merger. However, at earlier times the slope of the mass-transfer curve produced by the grid-code simulation does not match the slope of the curves produced by the SPH simulations. At the end of the initial phase of driving, the value of $|\dot{M}_{\text{D}}|$ in the grid-code simulation is also somewhat lower than the value of $|\dot{M}_{\text{D}}|$ in the SPH simulation. This is the first indication that, at relatively low mass-transfer rates, the simulations conducted with our two different numerical techniques generate results that are quantifiably different from one another. Figure 3a also shows that, while the blue and red curves illustrating the behavior of $q(t)$ and $J_{\text{A}}(t)$ overlap at late times, they do not lie precisely on top of each other at earlier times. For both of these binary parameters, this behavior probably reflects the discrepancy already noted in mass-transfer rates at early times.

The second indication that simulations conducted with the two different numerical codes generate results that are quantifiably different from one another comes from the bottom panel on the

right-hand side of Figure 3a, which illustrates the behavior of the spin of the donor star. In the grid code, J_D slowly but steadily decreases up until the moment of merger, whereas in the SPH code (at both resolutions) J_D initially increases, then decreases for a while, before increasing dramatically at the moment of merger. Overall, the Q1.3P simulation does not appear to be seriously impacted by this discrepancy in the behavior of $J_D(t)$. This is likely because the donor stores less than 10% of the system’s total angular momentum and, because $q_0 > 1$, the system is doomed to merge, independent of the precise treatment of spin-orbit coupling.

3.1.2. Q0.7P Model Simulations

As is recorded in Table 2, we carried out three separate polytropic simulations of binary systems having an initial mass ratio of $q_0 = 0.7$. Simulations conducted with the grid code (models *G1* and *G2*) were started from the initial model identified in Table 1 as Q0.7a while the simulation conducted with the SPH code (model *S1*) was started from the initial model identified as Q0.7b. These initial models were very similar, but not identical to one another; for example, the two stars in model Q0.7b were constructed as $n = 3/2$ polytropes having equal polytropic constants whereas the polytropic constants for the two stars in model Q0.7a were slightly different from one another. For both of the Q0.7 initial models, it is the less massive star that has the larger radius and hence these systems are closer analogs to low-mass (nonrelativistic) double white dwarf binaries near the anticipated stability limit for a polytropic equation of state with $n = \frac{3}{2}$ of $q_{\text{crit}} = \frac{2}{3}$. Simulations *G1* and *G2* differed from one another only in the duration of the initial phase of driving: *G2* was driven for $1.70P_0$ while *G1* was driven for $2.28P_0$. Model *S1* was driven for $1.0P_0$ and was conducted with $100k$ SPH particles.

As Figure 4a illustrates, the time-variation of key binary parameters exhibited by the various Q0.7P simulations was very similar and resembled the time-variations seen in simulation Q1.3P. For example, throughout each simulation a and q steadily decreased while $|\dot{M}_D|$ steadily increased. We conclude that, as with the Q1.3P simulation, the Q0.7P simulation was dynamically unstable to mass transfer. It is not entirely appropriate to describe the Q0.7P simulation as a merger, however. As is shown in the accompanying movies – video04 from simulation Q0.7P_*G1*, video05 from simulation Q0.7P_*G2*, and video06 from simulation Q0.7P_*S1* – the core of the donor star does not ultimately plunge into the core of the accretor. Instead, the donor star tidally disrupts and its material is dispersed by differential rotation to form an extended disk surrounding the accretor.

The upper right-hand image shown in Figure 4b is the frame picked from the movie of grid-code simulation Q0.7P_*G1* (video04) just before tidal disruption of the donor is complete. Using this frame to define the “instant of merger,” we obtain $t_{\text{merge}} = 9.70P_0$ for simulation Q0.7P_*G1*. The bottom right-hand image in Figure 4b is the frame picked from the movie of SPH-code simulation Q0.7P_*S1* (video06) that most closely resembles the upper right-hand image. Using this frame to define the “instant of merger” we deduce that $t_{\text{merge}} = 11.51P_0$ for simulation Q0.7P_*S1*. In a similar manner we have deduced that $t_{\text{merge}} = 21.03P_0$ for grid-code simulation Q0.7P_*G2*. These merger

times are recorded in the third column of Table 3. The “instant of merger” frames selected from simulations Q0.7P_G1, Q0.7P_G2, and Q0.7P_S1 share a considerable amount of detail, although this claim is somewhat weaker than in our earlier comparison of the model Q1.3P simulations because, in the present case, the SPH simulation was conducted with only $100k$ particles.

The left-hand images in Figure 4b present frames from the movies of simulations Q0.7P_G1, Q0.7P_G2, and Q0.7P_S1 half an orbit ($\Delta t = -0.5P_0$) prior to t_{merge} . These images also display a high degree of quantitative similarity. The pairs of images in Figure 4b illustrate what a careful viewing of the relevant movies reveals: the two different numerical schemes produce very similar dynamical results, especially as the simulations each evolve through the phase of tidal disruption of the donor. Furthermore, a comparison of the top pair of images with the middle pair of images shows that the outcome of this particular simulation is relatively insensitive to the precise amount of driving that is applied in order to initially bring the surface of the donor into contact with its Roche lobe.

As was seen in the context of the Q1.3P simulations, the time of merger is different in the three Q0.7P simulations. It is not surprising that tidal disruption of the donor occurs earlier in grid-code model *G1* than in grid-code model *G2* because, in *G1*, the “driving duration” was longer and, hence, the donor was initially driven into deeper contact with its Roche lobe. As Figure 4a illustrates, all three Q0.7P simulations show very good agreement when the time-evolutionary behavior of various system parameters is displayed using the *shifted* time defined by equations (6) and (7).

Again, it is worth pointing out ways in which results from the grid-code simulations differ from results obtained from the SPH-code simulation. As Figure 4a shows, throughout the simulation the mass-transfer rate increases somewhat more rapidly in simulation Q0.7P_S1 (solid blue curve) than in simulations Q0.7P_G1 and Q0.7P_G2 (dashed and solid red curves, respectively). This behavior was seen as well in simulations Q1.3P and, again, probably explains why the $q(t)$ curves do not lie precisely on top of one another at early times. The curves that trace the time-dependent behavior of J_{orb} and J_A in the SPH-code simulation (blue curves) lie slightly below the (red) curves drawn from the grid-code simulations. This is almost certainly because, in this case, the initial models were not identical. While the blue curve describing the time-evolutionary behavior of J_D does not lie precisely on top of the red curves, the general shape of the curves derived from the two different numerical techniques appears to be more similar than was seen in Figure 3a for simulation Q1.3P.

We note that the short period ($\sim 1P_0$) oscillations that are visible in all $a(t)$ curves — see the upper left-hand panels of Figures 3a and 4a — arise because, in practice, none of the binary orbits is perfectly circular. The amplitude of the resulting “epicyclic oscillations” is determined, in part, by the duration of driving that was initially imposed on each model simulation. The absolute phases of the epicyclic oscillations generally do not — and should not be expected to — match when the $a(t)$ curves are plotted as a function of the *shifted* time.

3.1.3. Model Simulations Q0.5P and Q0.4P

We have simulated polytropic mass-transfer in three binaries with initial mass ratios $q_0 < q_{\text{crit}}$: Simulations Q0.5P with $q_0 = 0.500$ and polytropic simulations Q0.4a with $q_0 = 0.4085$ and Q0.4b with a similar $q_0 = 0.4203$. Parameters defining the initial properties of these systems are detailed in Table 1. As noted in Table 1, model Q0.5 most closely represents a double white dwarf binary with low mass components as the donor star is the less massive component. Models Q0.4a and Q0.4b are similarly semi-detached systems with the less massive star in contact with its Roche lobe but these particular models have an accretor with a radius too large for its mass to be on the white dwarf mass – radius relation. This exacerbates the role of direct impact accretion in this model. As column 5 of Table 2 documents, models Q0.5P_G1 and Q0.5P_S1 were both initially driven into contact at a rate of 1% per orbit for $2.7P_0$. The evolutionary behavior of model Q0.5P_G1 is presented in the movie identified as video07; for comparison, the model Q0.5P_S1 simulation is presented in video08. (Some results from simulation Q0.5P_G1 already have been presented as model Q0.5-Da in §5.2 of DMTF06.) As Table 2 also details, five separate Q0.4P simulations were carried out. Among this group, we begin by discussing models Q0.4P_G1, Q0.4P_G2, and Q0.4P_S1, which were initially driven into contact at a rate of 1% per orbit for $1.6P_0$. Simulations Q0.4P_G1 and Q0.4P_G2 differ in their numerical resolution where Q0.4P_G1 was evolved with $4M$ grid cells while simulation Q0.4P_G2 was performed with $47M$ grid cells, partly in an effort to establish convergence of results with the grid code and to measure the lowest initial mass transfer rate that can be established in a numerical simulation of a semi-detached binary. Movies showing the evolutionary behavior of these three models are labeled video09, video10, and video12, respectively. The left panel of Figure 5 displays the time-evolutionary behavior of a , q , $|\dot{M}_D|$, J_{orb} , J_A , and J_D from simulations Q0.5P_G1 and Q0.5P_S1. Analogous information is displayed in the right panel of Figure 5 from simulations Q0.4P_G1 (solid curves), Q0.4P_G2 (dashed curves) and Q0.4P_S1. In all of the Figure 5 plots, red curves present results from grid-code simulations and blue curves present results from the $1M$ -particle SPH-code simulations.

The Q0.5P and Q0.4P model simulations differ from the simulations discussed earlier (Q1.3P and Q0.7P) in one especially significant way: The binary separation, a , does not decrease monotonically with time. Instead, a decreases for only a brief period of time associated with the initially imposed episode of driving, then the system reaches some minimum separation, a_{min} , and a increases monotonically thereafter. After a begins to increase, the *qualitative* behavior of each system’s subsequent evolution appears to depend on the depth of contact that was established between the donor and its surrounding Roche lobe during the phase of driving, as well as the rate of mass transfer, $|\dot{M}_D|$, exhibited at the end of the phase of driving, which correlates with the depth of contact. Simulations in which sufficiently deep contact is established display a mass-transfer rate that continues to increase with time even as the system separates; hereafter, these will be referred to as “Case A” evolutions. If, on the other hand, the donor established mass-transfer rate grows for only a short period of time, reaches a maximum rate $|\dot{M}_{\text{max}}|$, then levels off or declines as the system separates; these will be referred to as “Case B” evolutions.

The dashed curves sketched in Figure 6 illustrate in a qualitative fashion how other key parameters of the Q0.5P and Q0.4P binary systems respond to a steadily increasing mass-transfer rate in “Case A” evolutions; the solid curves illustrate how these key parameters respond to the “Case B” behavior. In Case A evolutions (*e.g.*, simulation Q0.4P_S1), the system mass ratio drops at an ever increasing rate and the accretor steadily spins up, principally extracting angular momentum from the system’s orbit. After an initial phase during which the donor also spins up — perhaps related to the initial, brief period of imposed driving — the donor also steadily donates angular momentum to the accretor. In Case B evolutions (*e.g.*, simulation Q0.4P_G1), the accretor stops gaining spin angular momentum and the curves that trace the behavior of $q(t)$, $J_{\text{orb}}(t)$, and $J_{\text{D}}(t)$ each develop an inflection point, indicating a slowing of the *rate* at which q , J_{orb} , and J_{D} are declining. In some Case B evolutions, angular momentum is eventually returned to the donor.

Comparing the two grid-based evolutions Q0.4_G1 and Q0.4_G2, we find that the higher-resolution simulation Q0.4_G2 has significantly shallower slopes in all quantities plotted in Figure 5. The amplitude of epicyclic motion has been reduced and increasing the numerical resolution by roughly a factor of 10 has reduced the initial mass transfer rate by about a factor of two. One may have hoped for second-order spatial convergence in the mass transfer rate but the edge of the star (where mass transfer is initiated) is not in a “smooth” region of the flow and only linear convergence, as we have found, is to be expected. This fact offers additional evidence for the computational challenge of mass transfer evolutions. The peak mass transfer rate is similarly smaller in the evolution Q0.4_G2 compared to Q0.4_G1 and in the higher resolution simulation, the binary is still gently separating after evolving for more than 50 orbits.

In an effort to better understand how the duration of imposed driving affects the outcome of low q_0 model simulations, we again used both numerical codes to conduct polytropic simulations starting from initial model Q0.4 (see Table 1) but subjected the system to 1% per orbit driving for only $1.16P_0$. These are identified as simulations Q0.4P_G3 and Q0.4P_S2 in Table 2. (Some results from simulation Q0.4P_G3 already have been presented as “baseline simulation Q0.4A” in §3 of MTFD07; note that MTFD07 mistakenly state that the duration of driving in this model was $1.6P_0$. A movie showing the first $1.0P_0$ of this “baseline simulation” was published by MTFD07; here video11 carries the same simulation through $47P_0$). Key results from these two simulations are displayed as *dashed* curves in Figure 7 — the red and blue curves are, respectively, from the grid-code and SPH-code simulations. For comparison purposes, the *solid* red and blue curves displayed in Figure 5b have been redrawn in Figure 7. Both of the SPH-code simulations display characteristics of a “Case A” evolution whereas both of the grid-code simulations (the dashed and solid red curves) display characteristics of a “Case B” evolution.

Based on the trends seen in Figure 7, it seems likely that, by subjecting the initial model to a phase of driving that is even shorter than $1.16P_0$, the SPH code would produce an evolution with “Case B” characteristics. Alternatively, it seems likely that, by subjecting the initial model to a phase of driving that is even longer than $1.6P_0$, the grid code would produce an evolution with “Case A” characteristics. Via a set of grid-code simulations, MTFD07 have previously provided

evidence (see especially their Figure 4) that, as the donor star is initially driven into deeper and deeper contact with its Roche lobe, a transition can be made from simulations that exhibit “Case B” characteristics to simulations that display “Case A” characteristics.

Our analysis of Q0.4P and Q0.5P model simulations also suggests the following. If a simulation of binary mass transfer traverses a “Case B” evolutionary trajectory, the donor may detach from its Roche lobe and, in so doing, avoid merger or tidal disruption. Three of the grid-code simulations actually show the mass-transfer stream detaching from the accretor late in the simulation: Video07 shows the binary detaching in simulation Q0.5P_G1 at $t \approx 34P_0$; as video11 shows, starting from the same initial state but with a shorter episode of driving, the stream detaches later, at $46.5P_0$; and video09 shows the binary detaching in simulation Q0.4P_G1 at $t \approx 40P_0$. The corresponding SPH simulations (Q0.5P_S1 depicted in video08, and Q0.4P_S1 depicted in video12) do not confirm this outcome, but both of these simulations were stopped before completing even twenty orbits so in both SPH simulations we can, at best, claim that the ultimate fate of the binaries is undetermined.

3.1.4. *Box- and Triangle-Shaped Resonances*

As has already been mentioned, MFTD07 used the same grid code as we have used here to analyze the behavior of Q0.4P simulations that were subjected to a variety of driving rates and driving durations. In §4 of their paper, MFTD07 point out that in the vicinity of the accretor some of the models developed nonlinear-amplitude “equatorial distortions with [azimuthal mode numbers] $6 \geq m \geq 3$.” The configuration displayed here in the upper-right-hand corner of Figure 8 is precisely the same configuration that was shown in the lower-right-hand corner of MFTD07’s Figure 3. It shows that, at time $t = 15.5P_0$ in MFTD07’s Q0.4D simulation, the disk surrounding the accretor has a triangular shape. As the image in the upper-left-hand corner of our Figure 8 shows, at time $t = 13.9P_0$ in the same MFTD07 simulation, the disk surrounding the accretor has a box shape; the time-evolutionary transition between the box and triangular shapes is shown in the mpeg animation of simulation Q0.4D that accompanies the MFTD07 publication.

The bottom two images in Figure 8 have been drawn from our video12. They illustrate that analogous box- and triangular-shaped distortions developed around the accretor in SPH simulation Q0.4P_S1. The box-shaped distortion appears at time $t = 16.47P_0$ and the triangular-shaped distortion appears at time $t = 17.98P_0$. We were gratified to see these azimuthal distortions develop spontaneously in simulation Q0.4P_S1. It demonstrates that our two entirely different numerical techniques for simulating binary mass-transfer can encounter and follow with comparable fidelity the development of unexpected nonlinear-amplitude structures in the midst of a complex binary interaction.

Box- and triangular-shaped distortions are not apparent in our grid-code simulation (Q0.4P_G1) that was initially driven at the same rate and for the same duration as SPH-code simulation Q0.4P_S1. Conversely, a careful viewing of video07 shows development of box- and triangular-

shaped distortions in the grid-code simulation of model Q0.5P, whereas these distortions are not apparent in the corresponding SPH simulation (model Q0.5P_S1; see video08). We suspect – as did MFTD07 – that “standing wave” azimuthal distortions of this type are routinely excited in polytropic simulations as a result of dynamical interactions between the mass-transfer stream and the accretion disk. But the distortions do not grow to nonlinear amplitude, and therefore are not visible to the eye, unless $|\dot{M}_D|$ is sufficiently large. In this light, it is not surprising that our eyes are unable to detect box- or triangular-shaped distortions in video09 even though they are present in video12 because, for model Q0.4P, the mass-transfer rate is always higher in the “Case A” SPH simulation than in the “Case B” grid-code simulation (see the Figure 5b plot of the time-dependent behavior of $|\dot{M}_D|$). And it is not surprising that our eyes are unable to detect nonlinear amplitude, standing-wave distortions in video08 even though they are present in video07 because, for model Q0.5P, the mass-transfer rate remains relatively low in the SPH simulation whereas it grows to moderately high levels in the long, grid-code simulation (see the Figure 5 plot of the time-dependent behavior of $|\dot{M}_D|$).

3.2. Ideal Gas Simulations

Here we discuss and compare results from simulations that were carried out using an ideal gas (“I”) equation of state. The relevant simulations are labeled as Q1.3I, Q0.7I, Q0.5I, and Q0.4I along with a two-digit model identification suffix in the last 10 rows of Table 2. As with the polytropic simulations, in each case the structure of the binary system at time $t = 0$ was prescribed by one of the initially uniformly rotating, $n = 3/2$ polytropic binary models identified in Table 1. Also as was done in the case of the polytropic simulations, at the start of a simulation, the donor star was driven into contact with its Roche lobe by artificially draining angular momentum from the system at a rate of one percent per orbit for the “driving duration” specified in column 5 of Table 2. Thereafter the system was evolved in a fully self-consistent fashion without further external influences. As is documented in column 4 of Table 2, all but one of the SPH simulations was carried out using 1 million ($1M$) particles; one model (Q0.7LS1) used 100 thousand ($100k$) particles. Every simulation performed with the grid code used a uniform cylindrical grid containing approximately 4 million grid cells.

In all of the ideal gas simulations, one structural feature develops that distinguishes each simulation from its polytropic counterpart: During the phase of mass transfer, a relatively hot, tenuous “envelope” develops around the accretor. This happens because the entropy of the material increases as the donor material passes through the shock front that is established where the accretion stream impacts the surface of the accretor. (The shock front also develops in all of the polytropic simulations but, by design, the entropy of the gas was not allowed to change.) This low-density envelope is easy to spot in the movie that accompanies each ideal gas simulation, especially if it is viewed alongside the movie from its polytropic counterpart; the lowest density, blue contour region is significantly extended in each ideal gas simulation. The accretion stream is also noticeably thicker

(hotter) in each ideal gas simulation, relative to its polytropic counterpart. And in some cases the hot tenuous envelope migrates over to the donor, establishing a classic “common envelope” in which the two stars are embedded. The image displayed in the top, right-hand corner of Figure 9 has been extracted at time $t = 17.75P_0$ from video17, which shows the ideal-gas simulation of model Q0.5 conducted with the grid code – specifically, simulation Q0.5I_G1. The common envelope structure is very apparent when compared with a frame (top, left corner of Figure 9) extracted from the middle ($t = 14.0P_0$) of video07, which shows the polytropic simulation conducted with the grid code that started from the same initial model (Q0.5) – simulation Q0.5P_G1. Similarly, the bottom two panels of Figure 9 display, for comparison, images from the polytropic simulation (video08; model Q0.5P_S1) and the ideal gas simulation (video18; model Q0.5I_S1) that started from initial model Q0.5 and were conducted using the SPH code.

In ideal gas simulations performed with the grid code, there is a tendency for a moderately extended “blue” atmosphere to develop around the binary components within the first orbit. This happens because, in the grid code, the region surrounding the initial binary system is not actually a vacuum but, rather, contains a very low density gas at a defined “floor” level. Once a simulation begins, this low-density gas free-falls down onto the donor, crashes into the surface supersonically, and heats up as a result. (The same dynamics occur in each corresponding polytropic simulation but a hot donor atmosphere does not result because, again by design, the entropy of the gas was not allowed to increase as it crashed into the stellar surface.) By contrast, an extended atmosphere does not typically develop around the donor during the first orbit of most SPH simulations because the region surrounding the binary system initially contains no material.

3.2.1. Q1.3I Model Simulations

We carried out two separate ideal-gas simulations of binaries that had an initial mass ratio $q_0 = 1.323$. In both cases the model was driven at a rate of 1% per orbit for $2.0P_0$ in order to initiate mass transfer. Whether the simulation was conducted using the grid code (model G1) or the SPH code (model S1), the Q1.3I simulation was found to be dynamically unstable to mass transfer. As Figure 10a illustrates, throughout both simulations, the binary separation (a) and system mass-ratio (q) steadily decreased while the donor mass-transfer rate ($|\dot{M}_D|$) steadily increased. As is shown in the accompanying movies – video13 from simulation Q1.3I_G1, and video14 from simulation Q1.3I_S1 – independent of the chosen numerical technique the two stars ultimately merged violently in the sense that the highest density “core” region of the donor was observed to collide and combine with the highest density “core” region of the accretor.

There is very little need for us to elaborate further regarding the behavior and outcome of these simulations because they resemble very closely our polytropic simulations that started from the same initial models. The time-dependent behavior of the six system parameters displayed in Figure 10a is very similar to the behavior of the same parameters as displayed in Figure 3a from the corresponding polytropic simulations; and the “merger” images shown in Figure 10b

from simulations Q1.3L_G1 (top) and Q1.3L_S1 (bottom) are nearly indistinguishable from the corresponding merger images that were drawn from our polytropic simulations and shown earlier in Figure 3b. Upon close examination, merger images from the ideal gas simulations show a somewhat more extended “blue” envelope than in the polytropic case. But this tenuous atmosphere did not significantly influence the overall dynamics of the merger.

It is worth pointing out that, while the merger time was nearly identical for simulations Q1.3L_S1 and Q1.3P_S1 – that is, for both the ideal-gas simulation and the polytropic simulation as produced by the SPH code – the merger times for simulations Q1.3L_G1 and Q1.3P_G1 differed by more than $3P_0$. This is reflected in, for example, a longer period of time for the mass transfer rate to grow in the grid evolution shown in Figure 10a compared to the polytropic evolution in Figure 3a. This delay is likely related to the moderately extended, tenuous “blue” atmosphere that developed in the star’s Roche lobes in the grid-code, but not the SPH, simulation. A tenuous atmosphere appears early in video13 but is absent in the polytropic simulation shown in video01 and SPH clearly does not suffer from this artifact in either polytropic (video02) or ideal gas (video14) evolutions. With the relatively long driving time required to bring the donor in to contact with its Roche lobe, the simulation Q1.3I_G1 is bringing a lower density, higher temperature atmosphere into contact as compared to the polytropic simulation Q1.3P_G1.

3.2.2. Q0.7I Model Simulations

As part of our comparison, we conducted two simulations of the binary with an initial mass ratio of $q_0 = 0.7$ and as with the Q0.7P simulations both numerical techniques find that the mass transfer grows with time leading to a tidal instability that disrupts the donor star. As detailed in Table 2, the SPH simulation was carried out with a resolution of $100k$ particles and was driven into contact for only $1.0P_0$ while the grid simulation was conducted with approximately 4 million grid cells and was driven into a deep contact with a driving period of $2.28P_0$.

The effects of a lower resolution in the SPH simulation Q0.7L_S1 are reflected in Figure 11a in both the higher epicyclic amplitude of the orbit and the higher mass transfer rate initially. As we have seen previously, the higher mass transfer rate dictates a shorter time to merger for the Q0.7L_S1 compared to the Q0.7L_G1 simulation but once we have adjusted the time series of data from Q0.7L_S1 with a zero point shift of $t_{zpt} = 2.33P_0$ both numerical techniques yield a very similar solution for the tidal instability that destroys the donor star. Images drawn from these simulations during tidal instability are shown in Figure 11b.

As in the Q1.3I discussion, the SPH code gives nearly identical results regardless of the assumed equation of state. For the grid code, the results are more similar to the polytropic evolutions and noticeably, there is no delay in the time to merger and the mass transfer rate does not stall in the ideal gas simulation. One difference that can be discerned in the grid-based evolution Q0.7I_G1 is that the spin angular momentum of the donor star remains constant until the donor is disrupted

whereas in the polytropic evolutions Q0.7P_G1 and Q0.7P_G2, the donor’s spin angular momentum declines gently before rising steeply as the donor star is disrupted.

3.2.3. Model Simulations Q0.5I and Q0.4I

To complete our testbed of simulations, we have repeated simulations of the two low mass ratio models with an ideal gas equation of state yielding the six simulations Q0.5I_G1, Q0.5I_S1, Q0.4I_G1, Q0.4I_G2, Q0.4I_S1 and Q0.4I_S2. The simulations of the Q0.5 model offer a good representation of a DD system as both components in the initial data share the same value of the polytropic constant (see Table 1). As the donor star was relatively far from contact initially, the system was driven for $2.7P_0$ in both the SPH and the grid-code simulations.

The SCF model Q0.4a is somewhat more complicated as the polytropic constants for the donor and accretor are not equal and the donor star is too large (compared to what would be the case with a zero-temperature white dwarf equation of state). The relatively large volume of the donor’s Roche lobe that is occupied by the star has important consequences for the outcome of the ideal gas simulations of this model. We have run this model four times, twice with each code where we have varied the initial depth of contact and hence the initial mass transfer rate. The simulations Q0.4I_G1 and Q0.4I_S1 were driven for $1.6P_0$ to establish contact while the simulations Q0.4I_G2 and Q0.4I_S2 were only driven for $1.16P_0$ to establish a more shallow initial contact.

Including the ideal gas equation of state introduces a new phenomenon into simulations of binaries with initial mass ratios below the cutoff for dynamically unstable mass transfer, q_{crit} . Namely, the accreting star will expand to the point that it also fills its Roche lobe forming a common envelope about both stars with the possibility that mass is lost from the binary through the outer Lagrange points (see the movies video17 and video18 as well as the still images in the bottom row of Figure 14). The incorporation of shock heating in the ideal gas equation of state introduces an additional, spurious effect in grid-based simulations. In an Eulerian treatment, no grid cell is allowed to be completely empty and a floor level of the mass density is maintained artificially even in regions that should clearly be vacant. At the start of a simulation, this material will begin to free-fall onto the binary system and shock heat as it crashes into the stars, heating their outer layer. As can be seen in the plot of mass transfer rate for the Q0.5I simulations in the left hand panel of Figure 12, the grid simulation Q0.5I_G1 emerges from the driving phase with a mass transfer rate that is approximately an order of magnitude higher than the SPH simulation Q0.5I_S1. The hotter envelope for the donor star in the grid-based simulation means that the common envelope phase where the separation varies about a constant mean value is longer than in the SPH simulation Q0.5I_S1.

The quasi-Lagrangian formulation in SPH does not suffer from the “vacuum” effects that arise in the grid code. In fact, there are indications that for the Q0.5I simulations that the SPH code is approaching a different solution than the common envelope followed by tidal instability

found with the grid-based simulation Q0.5I_G1. In the grid-based simulation a common envelope phase is established where the mass transfer rate grows with relatively little change in the orbital separation or the distribution of angular momentum between the orbital motion and the spin of each component. This phase is followed by a rapid tidal instability where the orbital angular momentum plummets while the spin angular momentum of each star grows rapidly. In the SPH evolution of this model there is still a common envelope phase but the evolution seems to be approaching the tidal disruption of the donor star, not a tidal instability.

A similar pattern can be seen in the ideal gas simulations of the Q0.4a initial data. The right hand panel of Figure 12 shows data for the two simulations with a greater initial depth of contact (corresponding to a longer driving period of $1.6P_0$). The grid simulation Q0.4I_G1 (video19) is very short lived, the mass transfer rate grows rapidly and tidal instability destroys the donor star within approximately 12 orbits. In part this is due to the numerical artifact of the vacuum discussed previously as well as the relatively large fraction of the accretor’s Roche lobe that is occupied initially (meaning that a common envelope forms rapidly and mass exchange and mass loss effects set in rapidly). For the same initial driving period of $1.6P_0$ in simulation Q0.4I_S1 (video21), we again find a common envelope phase followed by tidal instability. Note however that without the artificial heating of the envelope, the SPH simulation is qualitatively similar to the polytropic simulation. The same is not true for our grid-based simulations however.

As shown in Figure 13, reducing the initial driving period extends the life of the binary for both codes. Please note that as described in the appendix, the mass transfer rate that is plotted is smoothed with a boxcar function with a width of three initial orbital periods meaning that mass transfer rate at the end of driving is not represented for the Q0.4I_G2 simulation in Figure 13. With a shallower initial depth of contact, the grid-based code now finds tidal instability of the donor occurring later in the simulation. With the SPH code however, the mass transfer rate has turned over – perhaps indicating that it may avoid destruction of the donor star and reach detachment with a longer run.

Figure 14 shows several time slices around the tidal instability event from the simulations Q0.4I_S1 and Q0.4I_G1. While the initial mass transfer rates and subsequent time scales are different between the two runs, there is detailed agreement between the structure of the common envelope, the tidal disruption of the donor star and the resulting disk of debris wrapped around the accretor.

4. Summary and Conclusions

For reference, we have summarized our conclusion for the fate of each simulation (when it could be determined given existing data) in the seventh column of Table 3. Possible outcomes range from the donor star detaching from its Roche lobe, the destruction of the binary through tidal instability (the spin angular momentum of each component grow rapidly while the orbital

angular momentum crashes), and the tidal disruption of the donor star (where the spin angular momentum of the donor remains relatively constant while the donor is tidally shredded). These outcomes are in some instances modified by the formation of a common envelope phase which can be identified as relatively steady orbital separation while the mass transfer rate grows.

The standard linear analysis of the dynamical stability of mass transfer in binaries with spherical components, in the Roche approximation, and driven by angular momentum losses (AML) (Rappaport et al. 1982; Soberman et al. 1997; Marsh et al. 2004; Gokhale et al. 2007), reveals two critical values of the mass ratio $q = M_D/M_A$: 1) if $q > q_a$, the effect of the mass transfer by itself will tend to reduce the binary separation, whereas it will tend to expand the binary otherwise; 2) if $q < q_{\text{crit}}$, the mass transfer is stable and will tend toward a secular value proportional to the AML rate, whereas the mass transfer will be unstable otherwise and grow dynamically for $q > q_{\text{crit}}$.

In the simplest case of conservative mass transfer (no loss of mass from the system) and neglecting the effects of tidal distortions and spin-orbit coupling, $q_a = 1$, and as already stated earlier, for donors obeying a polytropic EOS with $n = 3/2$, $q_{\text{crit}} = 2/3 < q_a$. Therefore, based on these critical mass ratios, the expected evolutionary behavior of interacting, polytropic binary systems can be divided into three broad categories, depending principally upon whether the system’s initial mass ratio q_0 falls above q_a , in between q_{crit} and q_a , or below q_{crit} . If $q_0 > q_a$, both AML and mass transfer contribute to shrinking the binary separation and driving the donor into deeper contact. Thus we expect the mass-transfer rate to increase monotonically while the separation decreases monotonically, probably leading to a merger. If $q_{\text{crit}} < q_0 < q_a$, AML will shrink the binary initially, but once contact is established, the dynamically unstable mass transfer is expected to grow, halt the contraction and then rapidly increase the separation. This behavior resembles closely the “Case A” evolutions of §3.1.3. As the mass and density of the donor decrease, we may expect that the donor material is tidally wrapped around the accretor. Finally, if $q_0 < q_{\text{crit}}$, after AML shrinks the binary into contact, the mass transfer will settle toward the expected secular equilibrium value. If, as in our case, $q_{\text{crit}} < q_a$, the expectation is that the orbit will settle into a secular expansion, with the donor, and thus the binary, surviving. This behavior resembles in part the “Case B” evolutions of §3.1.3.

Before attempting to understand our simulations in terms of the above simple classification, we must note some important differences between the assumptions made in the standard treatments and the conditions prevalent in the simulations. First, driving by AML is only applied initially for varying lengths of time and then switched off. This results in varying degrees of contact and mass-transfer rates at the point AML ceases. Thereafter, the system’s evolution is driven by instabilities and any residual low-level angular momentum losses or gains due to numerical artifacts or mass loss from the system. Second, tidal distortions and spin-orbit coupling occur naturally during the simulation and these dominate the simulation especially at late stages.

The numerical simulations described in this work demonstrate that systems in the first category (relatively large $q_0 > q_a$), following the onset of mass transfer, are dynamically unstable from the

outset. As the binary separation decreases, the mass-transfer rate monotonically increases and, in a finite time, the stellar components either merge or the donor tidally disrupts. On the other hand, once mass-transfer has been initiated in systems that have a relatively small $q_0 < q_a$, the binary separation will generally increase with time. Our two distinctly different CFD algorithms agree on the evolutionary outcome of these dynamically unstable systems. For example, in every one of our Q1.3 simulations, the cores of the two stars merge; whereas, in every Q0.7 simulation, the donor tidally disrupts and material from the donor disperses to form a rotationally flattened disk around the accretor. As is illustrated by Figures 3b and 4b (and their associated animation sequences), this agreement is more than qualitative: detailed structures that arise during merger or tidal disruption events are present in simulations that are conducted with both codes.

Highly non-linear, transient structures such as the box- and triangle-shaped resonances in the Q0.4a polytropic evolutions have emerged in simulations with our two disparate codes as highlighted in Figure 8. These transitory equatorial distortions indicate that both techniques are yielding solutions remarkably close to one another in the parameter space of possible numerical solutions despite their different error terms, numerical artifacts, and fundamental representations of a fluid state. These resonance features represent a non-trivial verification of our codes.

For a given model, our two different CFD codes generally do not agree on the precise time of merger (or of tidal disruption), t_{merge} . But as is summarized in Table 3, even the same code will produce different values of t_{merge} when a simulation is repeated at a different code resolution or with a different driving duration. These apparent discrepancies arise because the precise value of t_{merge} is sensitive to the depth of contact that the Roche lobe makes with the donor star following the initial phase of driving. All other things being equal, a relatively brief phase of driving will result in relatively shallow contact, in which case the binary simulation will begin with a low mass-transfer rate and it will take the system a relatively long time to merge. If the phase of driving lasts longer, the simulation will begin with a higher mass-transfer rate and, as a result, the time to merger will be shorter. For a given driving duration, we have found that the time to merger is shorter in an SPH-code simulation than in a grid-code simulation. In effect, this implies that for a specified driving duration the Roche lobe establishes deeper contact with the donor star in the SPH code than in the grid code. We must emphasize, however, that the ultimate outcome of these simulations is not sensitive to code resolution or to driving duration. Also, as stated earlier, the outcome does not depend on the selected CFD algorithm: If the chosen binary system is dynamically unstable toward merger (or to tidal disruption of the donor), all simulations ultimately converge to the same solution.

Our collection of simulations demonstrates that the evolutionary outcome of systems in the third category (relatively small $q_0 < q_{\text{crit}}$) is sensitive to the depth of contact that the Roche lobe makes with the donor star during an initial phase of driving. (See especially the discussion associated with Figure 6.) If, for a given q_0 , the depth of contact is sufficiently deep, then the mass-transfer rate will monotonically increase even as the binary separation is increasing and, ultimately, the donor star will tidally disrupt. This is what has been referred to in §3.1.3 as “Case

A” evolutions. If, however, the depth of contact is initially sufficiently shallow, a “Case B” evolution will result, that is, the mass-transfer rate will eventually reach a maximum and, thereafter, will level off or decrease as the binary separation increases. For a specified q_0 and driving duration — at least within the range of parameters we have explored in this low q_0 category, using a polytropic equation of state — simulations conducted with the SPH code tend to result in “Case A” simulations whereas simulations conducted with the grid code tend to result in “Case B” simulations. As a consequence, we find that the donor star tends to tidally disrupt in simulations conducted with the SPH code whereas the donor tends to survive in simulations conducted with the grid code, at least for the length of time we’ve been able to follow the simulations. A given system can therefore appear to be either unstable or stable, depending on the CFD algorithm that has been selected to perform the simulation. This is not a particularly desirable result. But it is understandable and it is consistent with the behavior deduced from our analysis of relatively large q_0 simulations. For a specified driving duration the Roche lobe typically establishes deeper contact with the donor star in the SPH code than in the grid code. In turn, deeper contact will tend to result in a “Case A” rather than a “Case B” evolution.

When we compared polytropic and ideal gas simulations of the same initial model we noted the formation of a low-density hot envelope and the greater thickness of the stream both as a result of the higher temperature of the gas in the ideal gas case. However, while the higher temperature of the envelope resulting from the accretion shock appears both in the SPH and grid simulations and is likely a true physical effect, the dissipation of energy due to “vacuum” material settling on the binary during the first orbit is only present in grid simulations and should be considered a spurious effect. The spurious heating generates early on a hotter, thicker atmosphere, which allows a wider stream and enhances the mass transfer. This tends to speed up the simulation, sets it on a more unstable pathway and makes it difficult for the system to return to stability when the donor is near contact initially. This has little or no effect on the ultimate fate of the Q1.3I and Q0.7I models, but it does affect the simulation of the models Q0.5I and Q0.4I. In particular, the higher initial mass transfer rate in the grid simulations for the Q0.4I model results in a faster tidal disruption for the grid simulations than in the SPH simulations. This is in contrast to most of the other cases presented here, where the mass transfer rate in SPH simulations is higher yielding also a faster final outcome.

An obvious difficulty in the interpretation of our low q_0 simulations arises in connection with the uncertainty in the effective value of q_{crit} because of the noted differences between the assumptions made in analytic treatments and the “reality” of the simulations. Since direct impact occurs in our simulations, but also disk-like flows arise around the accretor, we may guess that the effective value is somewhere in the range $0.22 < q_{\text{crit}} < 2/3$. However, tidal effects are obvious in the images and movies presented here, and our simulations suggest that the ultimate fate of the low q_0 systems may well depend on the depth of contact achieved in the initial driving into contact. The levels of mass transfer in the simulations exceed the likely levels in real systems by many orders of magnitude. This may not be important for systems that are expected to be dynamically unstable, but caution

should be exercised when interpreting results for marginally unstable systems.

In summary, we conclude that aside from understandable shifts in the times taken by the same models evolved with SPH and grid hydrodynamics to reach the same evolutionary stages, and the split into Case A/B evolutions for low q_0 systems, the agreement between the results produced by our codes is remarkably close in the final outcomes and during intermediate evolutionary stages.

We acknowledge valuable interactions that we have had with Dominic Marcello, Kundan Kadam, and Zachary Byerly. In addition, we would like to thank the anonymous referee for their very careful and thoughtful review of our manuscript. This work has been supported, in part, by grants AST-0708551, NSF CREATIV grant AST-1240655, and DGE-0504507 from the U.S. National Science Foundation and, in part, by grant NNX07AG84G from NASA’s ATP program. This research also has been made possible by grants of high-performance computing time on the TeraGrid (MCA98N043), at LSU, and across LONI (Louisiana Optical Network Initiative). This material is based upon work supported by the National Science Foundation under Grant No. ACI-0338618l, OCI-0451237, OCI-0535258, and OCI-0504075. This research was supported in part by the Indiana METACyt Initiative. The Indiana METACyt Initiative of Indiana University is supported in part by Lilly Endowment, Inc. This work was supported in part by Shared University Research grants from IBM, Inc., to Indiana University. This material is based upon work supported by the National Science Foundation under Grant No. CNS-0521433.

A. Diagnostics

In an effort to quantitatively compare results from our various simulations of binary mass-transfer events, we have tracked the time-evolutionary behavior of a set of six key binary system parameters: Orbital separation, a , binary mass ratio, q , mass-transfer rate of the donor, \dot{M}_D , orbital angular momentum, J_{orb} , and spin angular momentum of the accretor, J_A , and donor, J_D . For each set of model simulations — for example, the simulations labeled Q1.3P that are discussed in §3.1.1 and illustrated in Figure 3a — the time-evolutionary behavior of each parameter has been illustrated by showing curves of the variation of each parameter versus time. The units that have been used in each plot are as follows: q is naturally dimensionless in both codes; a , J_{orb} , J_D , and J_A are in code units (see Table 1); time is normalized to the binary system’s original orbital period, P_0 ; and \dot{M}_D has been normalized by a mass transfer rate corresponding to the initial mass of the donor in the time span of the initial orbital period, that is,

$$\dot{M}_{\text{norm}} \equiv \frac{\dot{M}_D(t=0)}{P_0}. \quad (\text{A1})$$

For each model, the value of this normalization quantity also can be determined from the information provided in Table 1.

The simulation data from both numerical techniques were analyzed with the same tools in an effort to ensure that results from both numerical schemes were viewed through the same quantities. We chose to use diagnostic tools that were initially developed to analyze data sets from the cylindrical coordinate-based grid-code simulations. In order to enable analysis of the SPH simulations with this same set of diagnostic tools, data sets from the SPH simulations for mass, velocity, etc. were mapped onto a Cartesian grid (using a nearest grid point algorithm). Time series data for the six key variables were then computed for each simulation as follows.

The maximum density location for each star is identified and the line of centers of the binary is assumed to run through the two density maxima. A plane is then constructed parametrically that is perpendicular to the line of centers and divides the computational domain into two regions (donor and accretor) near the inner Lagrange point to enable identification of fluid elements that belong to the donor or accretor. The mass of each component and the binary separation are then computed from simple volume integrals of the density and density-weighted position of each star. The volume integrals extend over the entire grid region ascribed as donor or accretor based on the dividing plane. The momentum and mass within a given grid cell are combined to give the three components of velocity for the material in each cell. The orbital angular momentum is then calculated from the center of mass position and velocity of the two stellar components while the spin angular momentum of each component is computed by referencing velocities to the relevant center of mass. The mass transfer rate is computed as the centered finite difference of the mass of the donor star with respect to time and is quite noisy. The mass transfer rates shown in the figures are smoothed using a sliding box car average with a width equal to three times the initial orbital period, P_0 . Hence the first data point for the mass transfer rate shown is at $1.5P_0$ after the start of the simulation.

REFERENCES

- Amaro-Seoane, P., Aoudia, S., Babak, S., Binétruy, P., Berti, E., Bohé, A., Caprini, C., Colpi, M., Cornish, N. J., Danzmann, K., Dufaux, J.-F., Gair, J., Hinder, I., Jennrich, O., Jetzer, P., Klein, A., Lang, R. N., Lobo, A., Littenberg, T., McWilliams, S. T., Nelemans, G., Petiteau, A., Porter, E. K., Schutz, B. F., Sesana, A., Stebbins, R., Sumner, T., Vallisneri, M., Vitale, S., Volonteri, M., Ward, H., & Wardell, B. 2013, *GW Notes*, Vol. 6, p. 4-110, 6, 4
- Badenes, C., & Maoz, D. 2012, *ApJ*, 749, L11
- Benz, W. 1990, in *Numerical Modelling of Nonlinear Stellar Pulsations Problems and Prospects*, ed. J. R. Buchler, 269–288
- Brown, W. R., Kilic, M., Hermes, J. J., Allende Prieto, C., Kenyon, S. J., & Winget, D. E. 2011, *ApJ*, 737, L23
- Cohl, H. S., Rau, A. R. P., Tohline, J. E., Browne, D. A., Cazes, J. E., & Barnes, E. I. 2001, *Phys. Rev. A*, 64, 052509
- Cohl, H. S., & Tohline, J. E. 1999, *ApJ*, 527, 86
- Dan, M., Rosswog, S., Brüggem, M., & Podsiadlowski, P. 2014, *MNRAS*, 438, 14
- Dan, M., Rosswog, S., Guillochon, J., & Ramirez-Ruiz, E. 2012, *MNRAS*, 422, 2417
- Diehl, S., Fryer, C., & Herwig, F. 2008, in *Astronomical Society of the Pacific Conference Series*, Vol. 391, *Hydrogen-Deficient Stars*, ed. A. Werner & T. Rauch, 221
- Diehl, S., Rockefeller, G., Fryer, C. L., Riethmiller, D., & Statler, T. S. 2012, *ArXiv e-prints*
- Diehl, S., & Statler, T. S. 2006, *MNRAS*, 368, 497
- D’Souza, M. C. R., Motl, P. M., Tohline, J. E., & Frank, J. 2006, *ApJ*, 643, 381
- Frank, J., King, A., & Raine, D. J. 2002, *Accretion Power in Astrophysics: Third Edition*, 398
- Fryer, C. L., Rockefeller, G., & Warren, M. S. 2006, *ApJ*, 643, 292
- Fryer, C. L., Ruitter, A. J., Belczynski, K., Brown, P. J., Bufano, F., Diehl, S., Fontes, C. J., Frey, L. H., Holland, S. T., Hungerford, A. L., Immler, S., Mazzali, P., Meakin, C., Milne, P. A., Raskin, C., & Timmes, F. X. 2010, *ApJ*, 725, 296
- Fryer, C. L., & Warren, M. S. 2002, *ApJ*, 574, L65
- Gokhale, V., Peng, X. M., & Frank, J. 2007, *ApJ*, 655, 1010
- Hachisu, I. 1986, *ApJS*, 62, 461
- Hachisu, I., Eriguchi, Y., & Nomoto, K. 1986, *ApJ*, 311, 214

- Han, Z. 1998, *MNRAS*, 296, 1019
- Herant, M. 1994, *Memorie della Societa Astronomica Italiana*, 65, 1013
- Iben, Jr., I., & Tutukov, A. V. 1984, *ApJS*, 54, 335
- Kilic, M., Brown, W. R., Allende Prieto, C., Kenyon, S. J., & Panei, J. A. 2010, *ApJ*, 716, 122
- Kilic, M., Brown, W. R., Kenyon, S. J., Allende Prieto, C., Andrews, J., Kleinman, S. J., Winget, K. I., Winget, D. E., & Hermes, J. J. 2011, *MNRAS*, 413, L101
- Marsh, T. R., Nelemans, G., & Steeghs, D. 2004, *MNRAS*, 350, 113
- Monaghan, J. J. 1992, *ARA&A*, 30, 543
- . 2005, *Reports on Progress in Physics*, 68, 1703
- Motl, P. M., Frank, J., Tohline, J. E., & D’Souza, M. C. R. 2007, *ApJ*, 670, 1314
- Motl, P. M., Tohline, J. E., & Frank, J. 2002, *ApJS*, 138, 121
- Nelemans et al. 2005, *A&A*, 440, 1087
- Nelson, A. F. 2006, *MNRAS*, 373, 1039
- Pakmor, R., Edelmann, P., Röpke, F. K., & Hillebrandt, W. 2012, *MNRAS*, 424, 2222
- Pakmor, R., Kromer, M., Taubenberger, S., & Springel, V. 2013, *ApJ*, 770, L8
- Pakmor, R., Springel, V., Bauer, A., Mocz, P., Munoz, D. J., Ohlmann, S. T., Schaal, K., & Zhu, C. 2016, *MNRAS*, 455, 1134
- Parsons, S. G., Marsh, T. R., Gänsicke, B. T., Drake, A. J., & Koester, D. 2011, *ApJ*, 735, L30
- Postnov, K. A., & Yungelson, L. R. 2006, *Living Reviews in Relativity*, 9, 6
- Rappaport, S., Joss, P. C., & Webbink, R. F. 1982, *ApJ*, 254, 616
- Raskin, C., Scannapieco, E., Fryer, C., Rockefeller, G., & Timmes, F. X. 2012, *ApJ*, 746, 62
- Raskin, C., Scannapieco, E., Rockefeller, G., Fryer, C., Diehl, S., & Timmes, F. X. 2010, *ApJ*, 724, 111
- Raskin, C., Timmes, F. X., Scannapieco, E., Diehl, S., & Fryer, C. 2009, *MNRAS*, 399, L156
- Soberman, G. E., Phinney, E. S., & van den Heuvel, E. P. J. 1997, *A&A*, 327, 620
- Staff, J. E., Menon, A., Herwig, F., Even, W., Fryer, C. L., Motl, P. M., Geballe, T., Pignatari, M., Clayton, G. C., & Tohline, J. E. 2012, *ApJ*, 757, 76

- Stone, J. M., & Norman, M. L. 1992, *ApJS*, 80, 753
- Thomas, P. A., & Couchman, H. M. P. 1992, *MNRAS*, 257, 11
- Wang, J., & White, S. D. M. 2007, *MNRAS*, 380, 93
- Warren, M. S., & Salmon, J. K. 1995, *Computer Physics Communications*, 87, 266
- Webbink, R. F. 1984, *ApJ*, 277, 355
- Young, P. A., Fryer, C. L., Hungerford, A., Arnett, D., Rockefeller, G., Timmes, F. X., Voit, B., Meakin, C., & Eriksen, K. A. 2006, *ApJ*, 640, 891
- Yungelson, L. R., Livio, M., Tutukov, A. V., & Saffer, R. A. 1994, *ApJ*, 420, 336
- Zhu, C., Chang, P., van Kerkwijk, M. H., & Wadsley, J. 2013, *ApJ*, 767, 164

Table 1. Initial (Polytropic) Binary System Parameters

Model	q	κ_D	$\rho_{0,D}$	R_D	κ_A	$\rho_{0,A}$	R_A	$\frac{R_A}{R_{\text{circ}}}$	M_{tot}	a_{sep}	$P_0 = \frac{2\pi}{\Omega_0}$	Analog ^a	Notes
Q1.3	1.323	0.0372	0.600	0.3508	0.0264	1.000	0.2674	2.602	3.090×10^{-2}	0.8882	29.74	MS	(1)
Q0.7a	0.700	0.02512	0.608	0.2865	0.0273	1.000	0.2694	2.302	2.371×10^{-2}	0.8394	31.20	WD	...
Q0.7b	0.69985	0.02	0.6	0.2383	0.02	1.3	0.2703	2.584	1.700×10^{-2}	0.75	31.70	WD	...
Q0.5	0.500	0.016	0.235	0.2670	0.016	1.000	0.2052	1.496	9.216×10^{-3}	0.8764	53.52	WD	(2)
Q0.4a	0.4085	0.01904	0.710	0.2898	0.03119	1.000	0.2437	1.768	2.399×10^{-2}	0.8169	29.75	WD	(3)
Q0.4b	0.4203	0.01989	0.740	0.2958	0.03222	1.000	0.2479	1.811	2.550×10^{-2}	0.8207	29.05	WD	...

^aStellar analog of polytropic binary where MS means fully-convective, low mass, main sequence stars and WD means a white dwarf where both components are low in mass compared to the Chandrasekhar limit.

^bInformation drawn from: (1) Table 4 of DMTF06; (2) Table 5 of DMTF06; (3) Table 1 of MFTD07.

Table 2. Simulation Prescriptions.

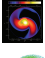

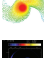
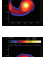
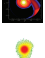
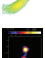
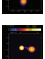
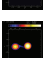
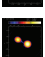
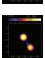
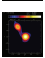

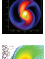
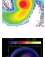
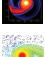
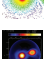
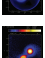
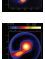
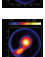
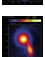

Simulation ^a	Model ID	Code	Resolution ^b	Driving Duration	Notes ^c
(1)	(2)	(3)	(4)	(5)	(6)
Q1.3P	<i>G1</i>	Grid	4 M	$2.0P_0$	(1)
	<i>S1</i>	SPH	1 M	$2.0P_0$	
	<i>S2</i>	SPH	100 k	$2.0P_0$	
Q0.7P	<i>G1</i>	Grid	4 M	$2.28P_0$	
	<i>G2</i>	Grid	4 M	$1.70P_0$	
	<i>S1</i>	SPH	100 k	$1.0P_0$	
Q0.5P	<i>G1</i>	Grid	4 M	$2.7P_0$	(2)
	<i>S1</i>	SPH	1 M	$2.7P_0$	
Q0.4P	<i>G1</i>	Grid	4 M	$1.6P_0$	(3)
	<i>G2</i>	Grid	47 M	$1.6P_0$	
	<i>G3</i>	Grid	4 M	$1.16P_0$	
	<i>S1</i>	SPH	1 M	$1.6P_0$	
	<i>S2</i>	SPH	1 M	$1.16P_0$	
Q1.3I	<i>G1</i>	Grid	4 M	$2.0P_0$	
	<i>S1</i>	SPH	1 M	$2.0P_0$	
Q0.7I	<i>G1</i>	Grid	4 M	$2.28P_0$	
	<i>S1</i>	SPH	100 k	$1.0P_0$	
Q0.5I	<i>G1</i>	Grid	4 M	$2.7P_0$	
	<i>S1</i>	SPH	1 M	$2.7P_0$	
Q0.4I	<i>G1</i>	Grid	4 M	$1.6P_0$	
	<i>G2</i>	Grid	4 M	$1.16P_0$	
	<i>S1</i>	SPH	1 M	$1.6P_0$	
	<i>S2</i>	SPH	1 M	$1.16P_0$	

^aSimulations labelled with “P” were evolved with a polytropic equation of state while simulations labelled with “I” utilized an ideal gas equation of state.

^bFor SPH simulations “resolution” means number of particles. For grid simulations, “resolution” means number of uniform cylindrical grid cells; $(N_R, N_\theta, N_Z) = (162, 256, 98)$, hence, 4.064M cells.

^cIdentical to model simulation (1) Q1.3-D, first discussed in §5.1.1 of DMTF06; (2) Q0.5-Da, first discussed in §5.2 of DMTF06; (3) Q0.4A, first discussed in §3 of MTFD07 – note: MTFD07 mistakenly state that driving was for $1.6P_0$.

Table 3. Simulation Diagnostics.

Simulation	Model	t_{merge}	t_{zpt}	Movie	Outcome ^a	Elaboration
(1)	ID	P_0	P_0	ID	(6)	(7)
Q1.3P	G1	12.38	0.00	 video01	TI	Binary merges at $12.4P_0$
	S1	7.57	+4.81	 video02	TI	Binary merges at $7.6P_0$
	S2	8.17	+4.21	 video03	TI	Binary merges at $8.2P_0$
Q0.7P	G1	9.70	0.00	 video04	TI	Donor disrupts at $9.7P_0$
	G2	21.03	-11.41	 video05	TI	Donor disrupts at $21.0P_0$
	S1	11.51	-2.11	 video06	TI	Donor disrupts $11.5P_0$
Q0.5P	G1	...	0.00	 video07	D	Binary detaches at $34P_0$
	S1	...	0.00	 video08	?	Undetermined after $14.6P_0$
Q0.4P	G1	...	0.00	 video09	D	Binary detaches at $40P_0$
	G2	...	0.00	 video10	?	Undetermined after $50.2P_0$
	G3	...	0.00	 video11	D	Binary detaches at $46.5P_0$
	S1	...	0.00	 video12	?	Undetermined after $18.3P_0$
	S2	...	0.00	...	?	(no movie)
	S2	...	0.00	...	?	(no movie)
Q1.3I	G1	15.54	0.00	 video13	TI	Binary merges at $15.5P_0$
	S1	7.69	+7.85	 video14	TI	Binary merges at $7.7P_0$
Q0.7I	G1	12.37	0.00	 video15	TI	Donor disrupts at $12.4P_0$
	S1	10.04	+2.33	 video16	TI	Donor disrupts at $10.0P_0$
Q0.5I	G1	...	0.00	 video17	CE + TI	Donor disrupts at $19.3P_0$
	S1	...	0.00	 video18	CE + TD?	Undetermined after $15.0P_0$
Q0.4I	G1	...	0.00	 video19	CE + TI	Donor disrupts at $8.3P_0$
	G2	...	0.00	 video20	CE + TI	Donor disrupts at $12.4P_0$
	S1	...	0.00	 video21	CE + TI	Donor disrupts at $21.4P_0$
	S2	...	0.00	...	?	(no movie)

^aTI = tidal instability; TD = tidal disruption; D = detaches; CE = common envelope

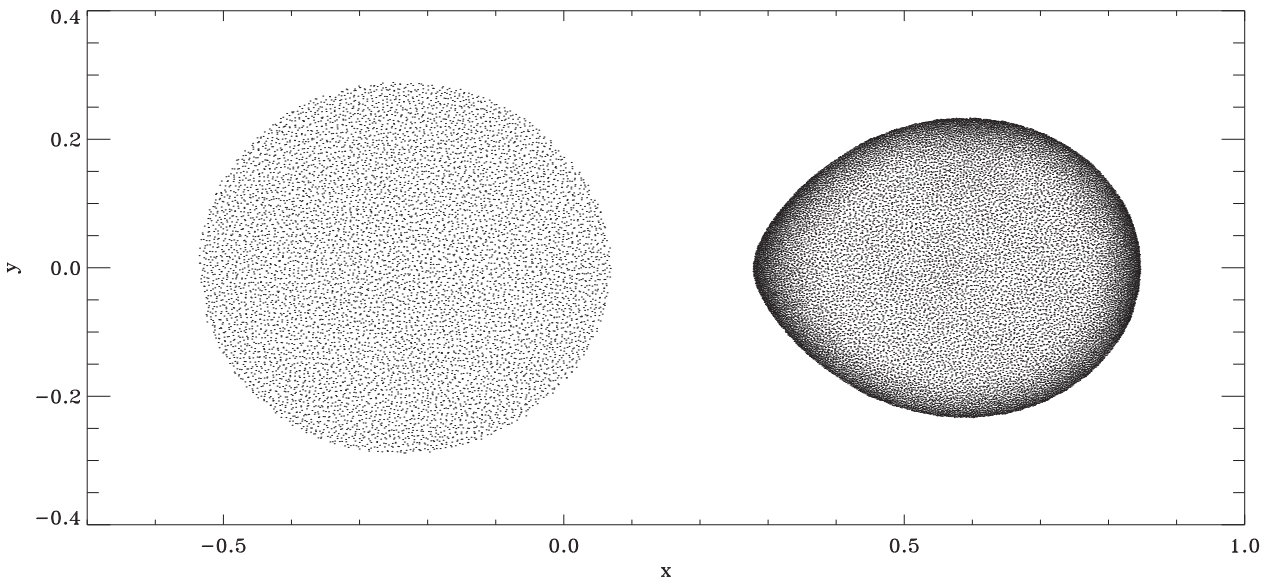


Fig. 1.— Slice through the meridional plane of the Q0.4a SPH setup, only particles within one smoothing length of the plane are shown. Note how the outer layers of the donor (right side) are much better resolved with a smaller particle spacing, whereas the accretor (left side) is set up with a uniform particle density.

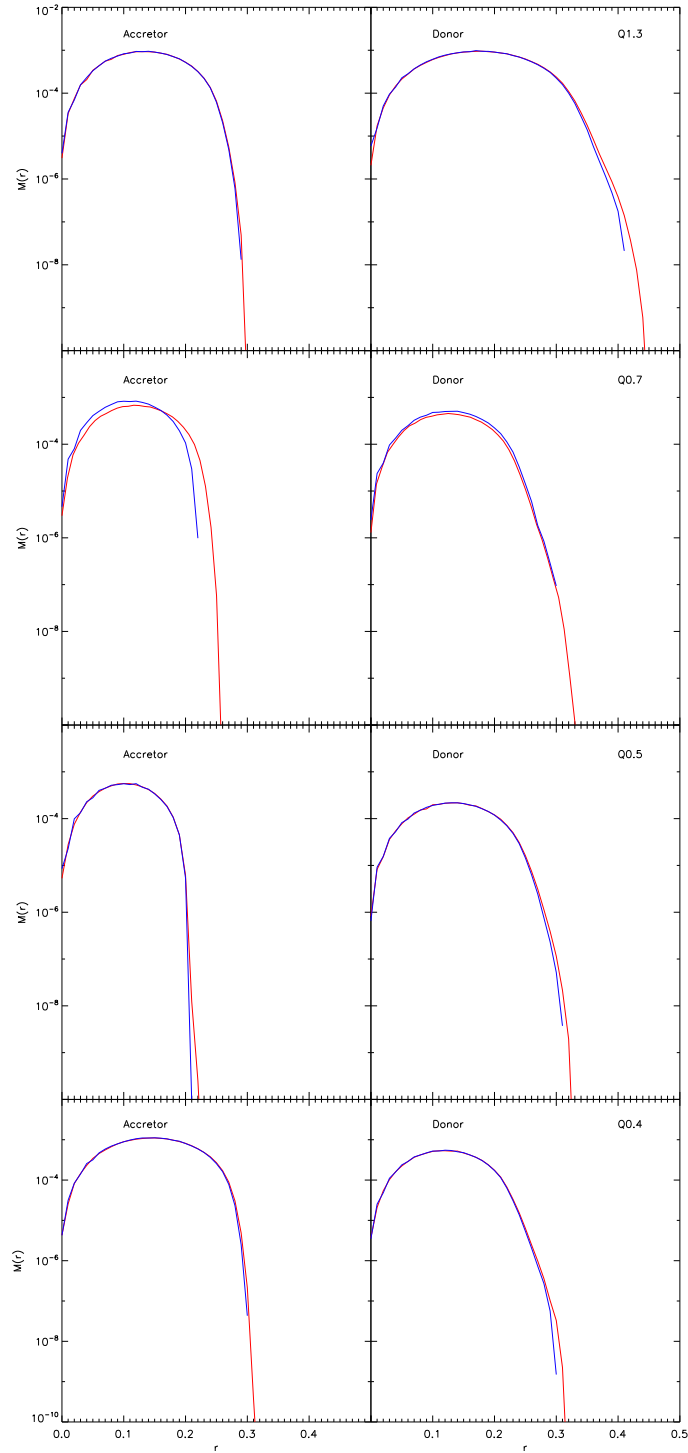


Fig. 2.— The mass profile of each stellar component taken from spherical shells centered on the center of mass of the accreting star (left column) and donor star (right column) for the four initial binary configurations Q1.3, Q0.7a and Q0.7b, Q0.5, and Q0.4a. The SPH initial data is plotted in blue while the Eulerian initial data is shown in red. Both codes are thus proceeding from very similar initial states and in the Eulerian representation, the donor stars (which nearly reach their Roche lobe) are resolved to a somewhat lower density level.

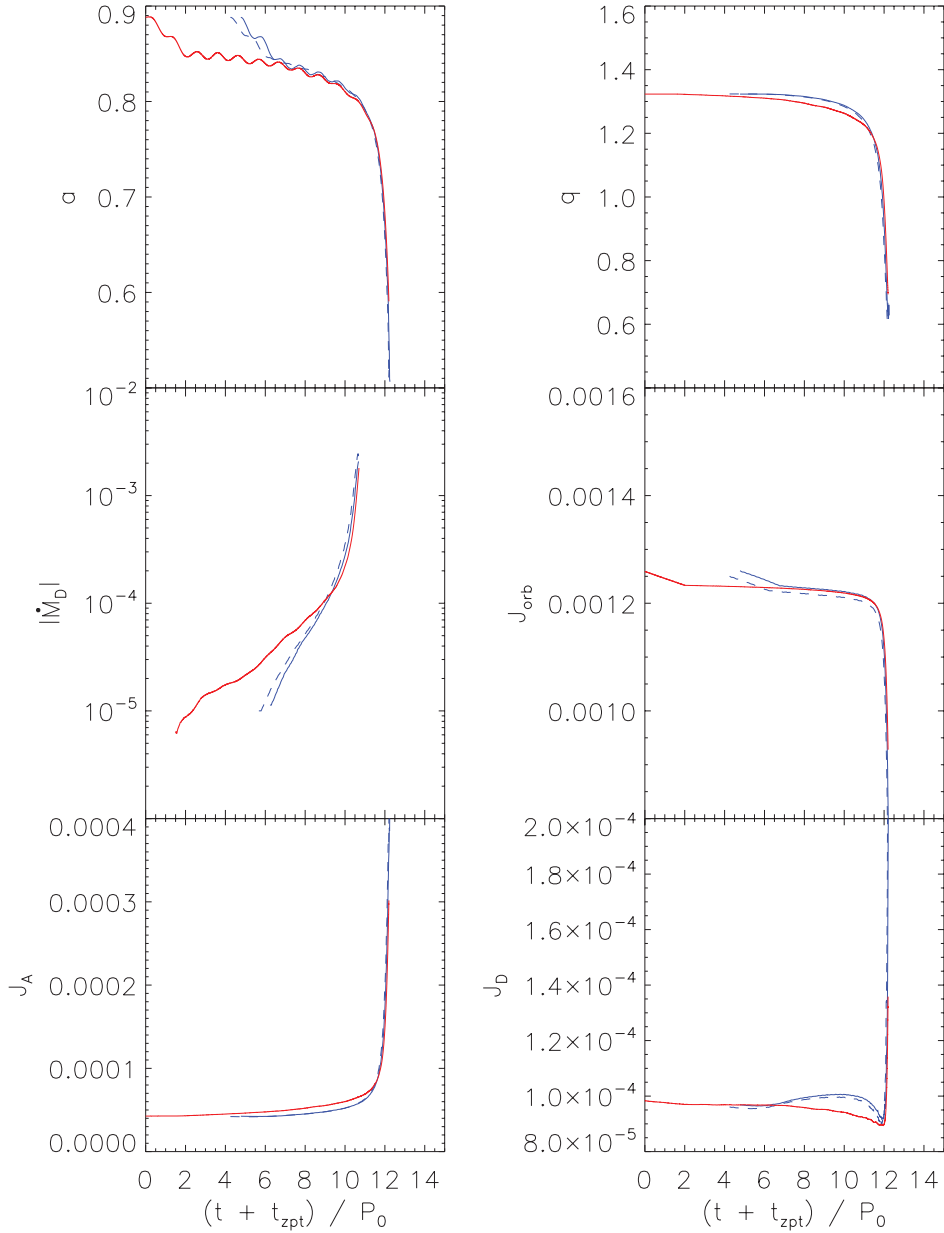


Fig. 3a.— Simulation Q1.3P. Curves show the time-dependent behavior of six system parameters — orbital separation, a , binary mass ratio, q , log of the donor mass-transfer rate, $|\dot{M}_D|$, orbital angular momentum, J_{orb} , and spin angular momentum of the accretor, J_A , and donor, J_D — as derived from models Q1.3P_G1 (solid red curves), Q1.3P_S1 (solid blue curves), and Q1.3P_S2 (dashed blue curves). For purposes of presentation, each curve has been terminated at a time shortly after the system mass ratio has dropped below $q = 0.7$ and curves from both SPH-code simulations include a zero-point shift in time, t_{zpt} , as detailed in column 4 of Table 3; units used along the vertical axis for each plot are defined in Appendix A.

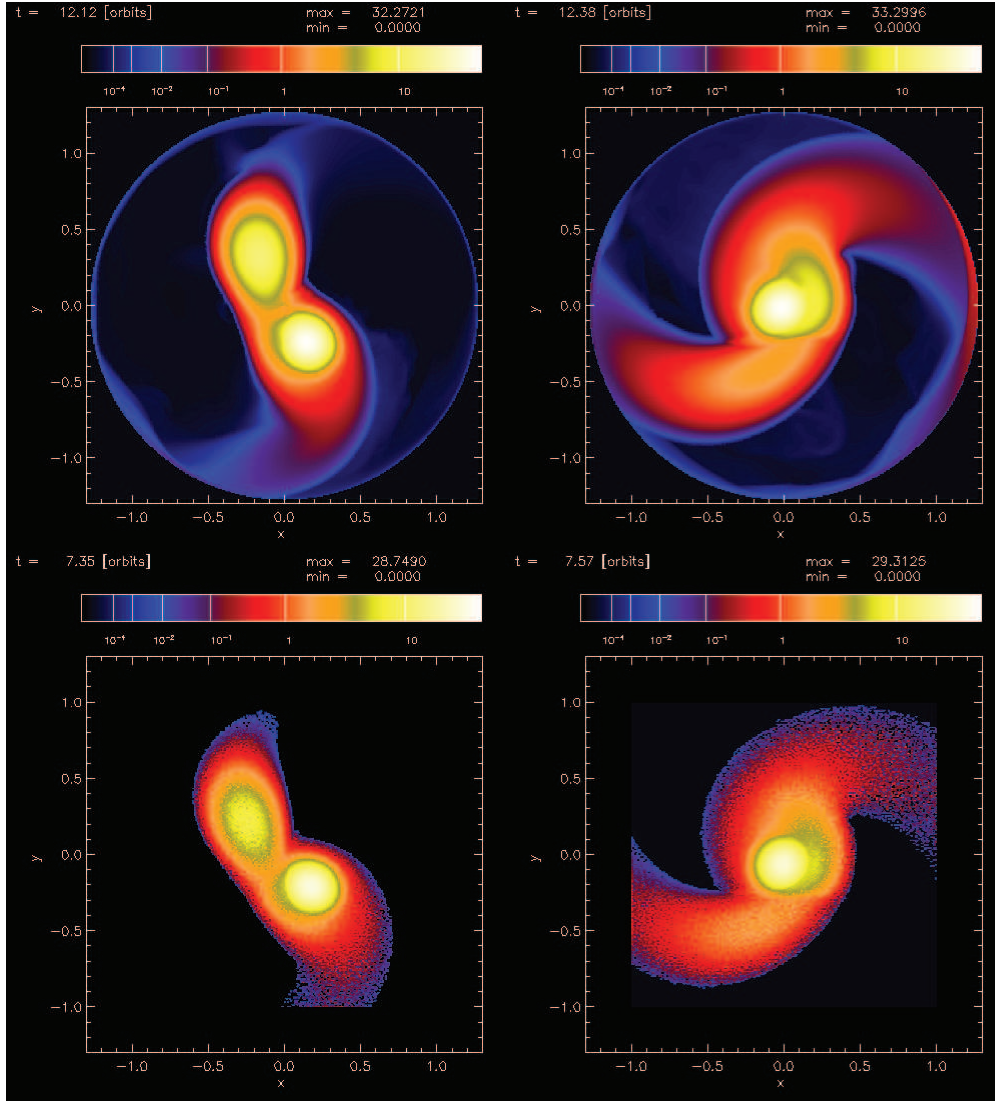


Fig. 3b.— Simulation Q1.3P. Images show contours of equatorial-plane column densities from model Q1.3P_G1 (top) and model Q1.3P_S1 (bottom) at two different points in time as the binary merger is occurring — specifically, *left-most images*: $t_{G1} = 12.12P_0$ and $t_{S1} = 7.35P_0$; *right-most images*: $t_{G1} = 12.38P_0$ and $t_{S1} = 7.57P_0$. The top two images have been extracted from video01 and the bottom two have been extracted from video02.

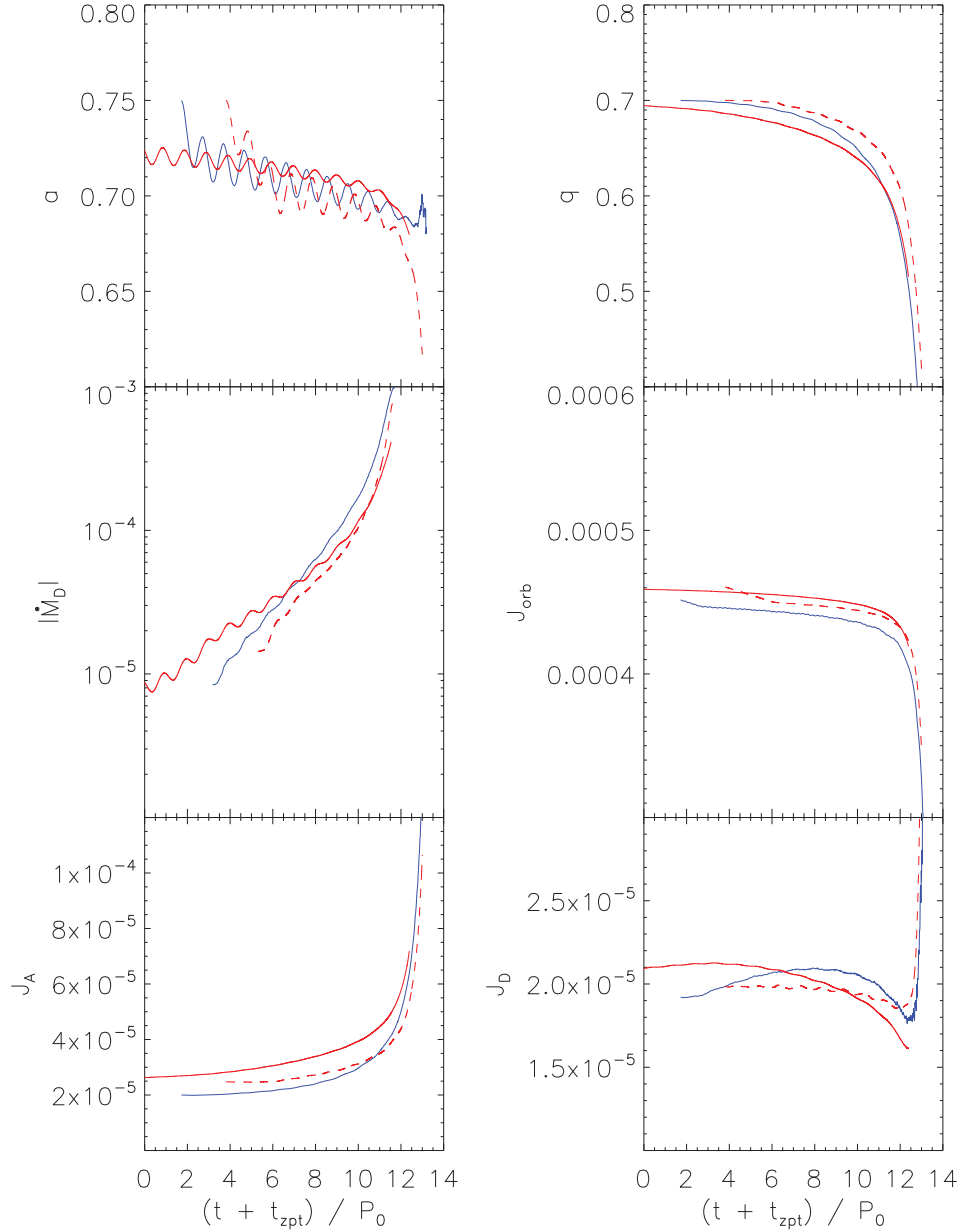


Fig. 4a.— Simulation Q0.7P. Curves show the time-dependent behavior of six system parameters — a , q , $\log |\dot{M}_D|$, J_{orb} , J_A and J_D — as derived from models Q0.7P_G1 (dashed red curves), Q0.7P_G2 (solid red curves), and Q0.7P_S1 (solid blue curves). For purposes of presentation, each curve has been terminated at the time in the simulation when the system mass ratio has dropped below $q = 0.4$ and curves from simulations Q0.7P_G2 and Q0.7P_S1 include a zero-point shift in time, t_{zpt} , as detailed in column 4 of Table 3; units used along the vertical axis for each plot are defined in Appendix A.

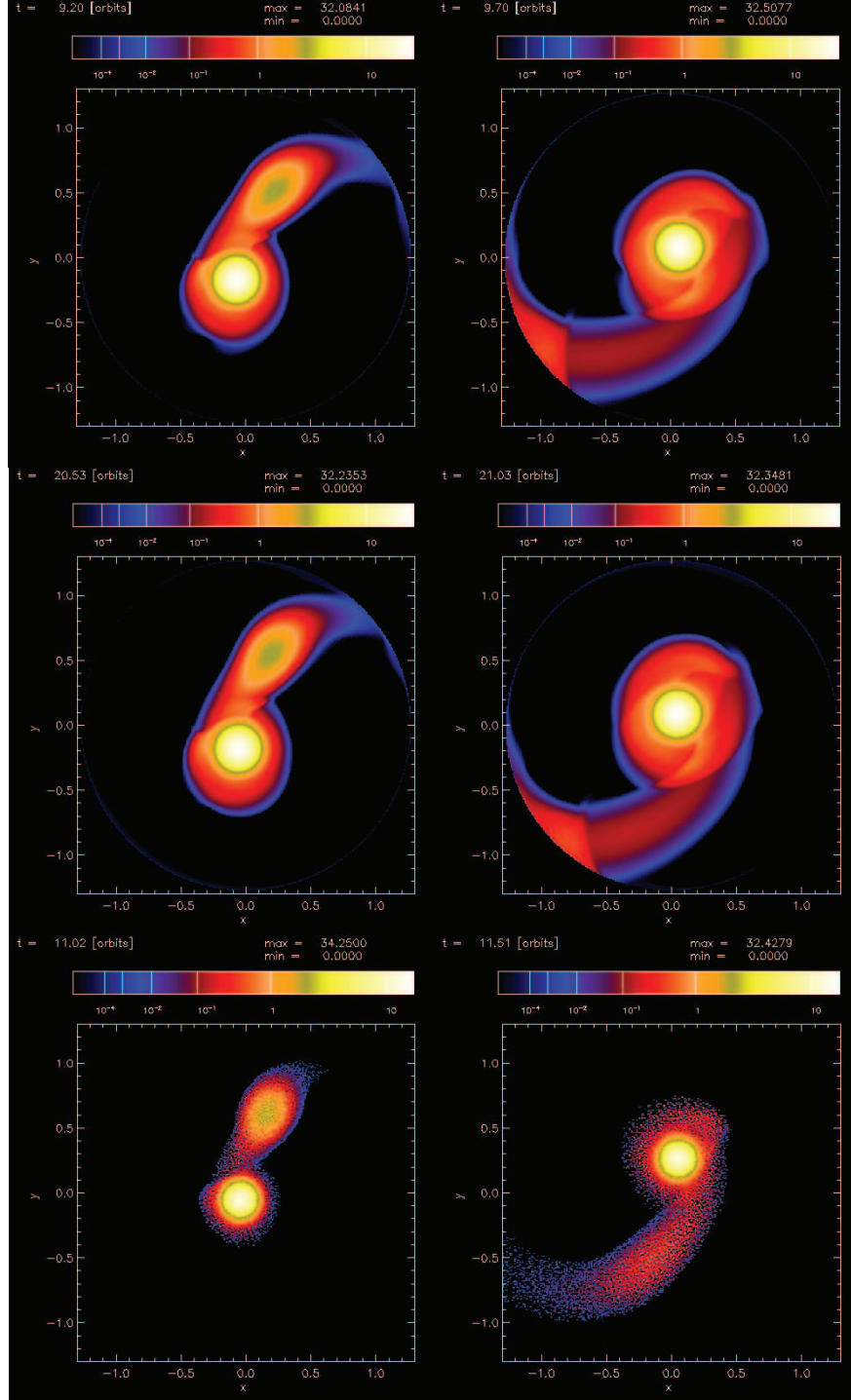


Fig. 4b.— Simulation Q0.7P. Images show contours of equatorial-plane column densities from simulation Q0.7P_G1 (top), Q0.7P_G2 (middle), and Q0.7P_S1 (bottom) at two different points in time as tidal disruption of the donor is occurring — specifically, *left-most images*: $t_{G1} = 12.92P_0$, $t_{G2} = 20.53P_0$, and $t_{S1} = 11.02P_0$; *right-most images*: $t_{G1} = 13.42P_0$, $t_{G2} = 21.03P_0$, and $t_{S1} = 11.51P_0$. The images displayed for simulations Q0.7_G1 (top), Q0.7_G2 (middle) and Q0.7_S1 (bottom) have been extracted from, respectively, video04, video05 and video06.

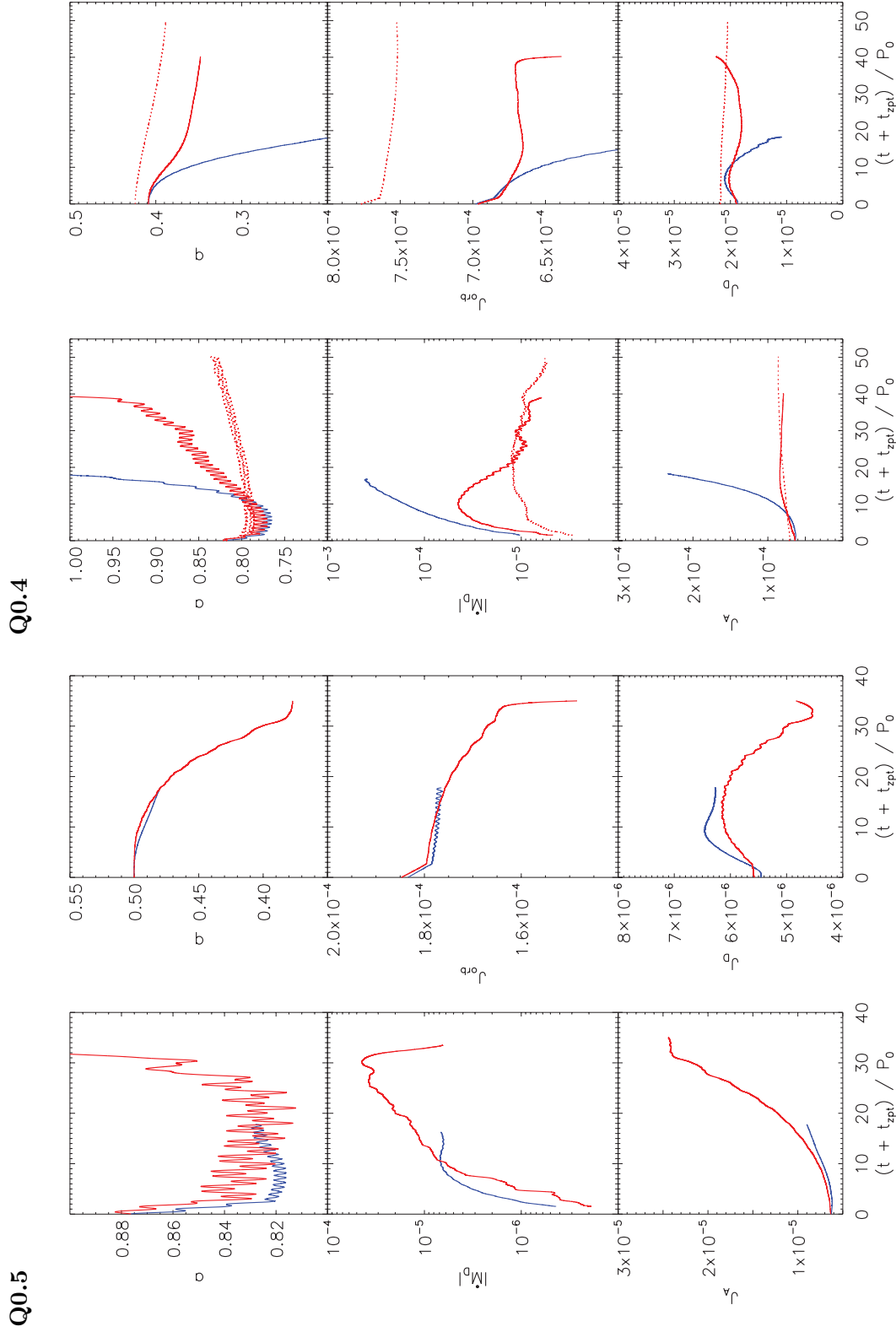


Fig. 5.— Simulations Q0.5P and Q0.4P. Curves show the time-dependent behavior of six binary system parameters: a , q , $\log|M_D|$, J_{orb} , J_A and J_D . The units used to normalize each quantity are defined in Appendix A. Left Panel: Results derived from models Q0.5P_G1 (red curves) and Q0.4P_G1 (blue curves). Right Panel: Results derived from models Q0.4P_G1 (red solid curves), Q0.4P_G2 (dashed red curves) and Q0.4P_S1 (blue curves).

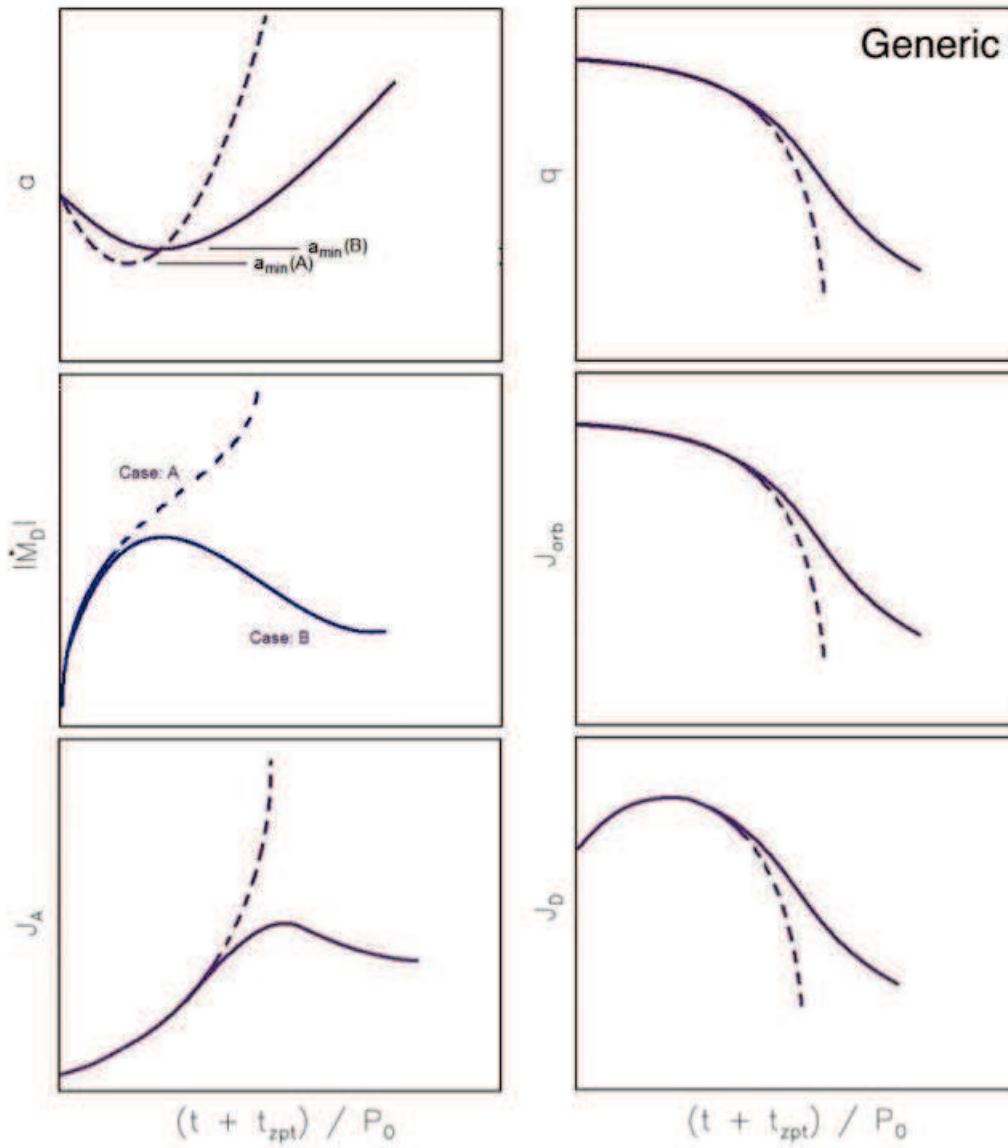


Fig. 6.— Accompanying the §3.1.3 discussion, a schematic illustration is presented of the generic, time-dependent behavior of six binary system parameters in “Case A” (dashed curves) and “Case B” (solid curves) evolutions.

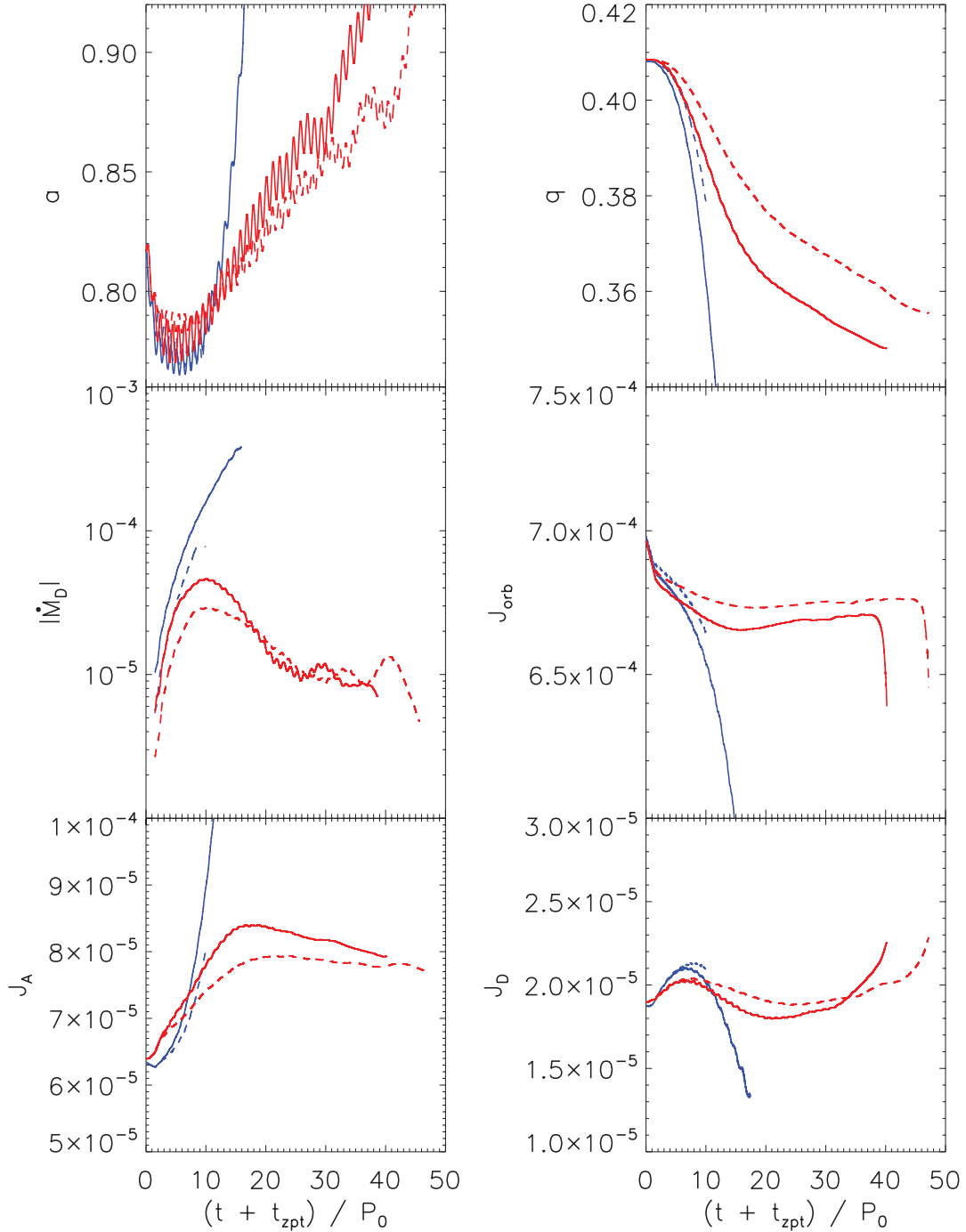


Fig. 7.— As in Figure 5b, curves show the time-dependent behavior of six binary system parameters from model simulations Q0.4P. Blue curves are derived from SPH-code simulations and red curves are derived from grid-code simulations. Solid curves exactly reproduce information provided in the left panel of Figure 5 from simulations that were driven into contact for $1.6P_0$; for comparison, dashed curves present results from simulations Q0.4P_G3 and Q0.4P_S2 that were driven into contact for only $1.16P_0$.

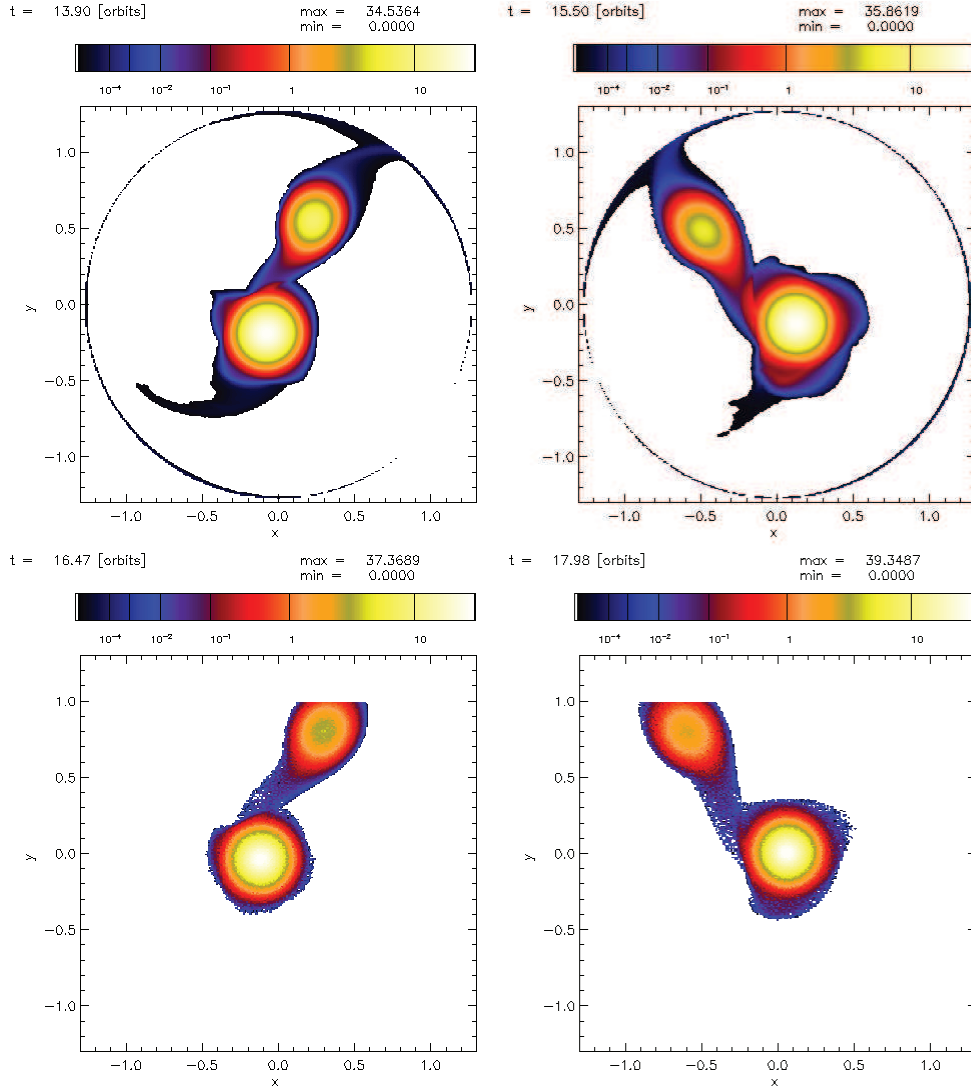


Fig. 8.— Equatorial-plane surface-density contours from (bottom) model Q0.4P_S1 and from (top) MFTD07’s model Q04D at two different times late in their simulations as similar nonlinear-amplitude box-like (left) and triangular-shaped (right) resonances are being excited in the equatorial-belt region of the accretor — specifically, *left-most images*: $t_{Q04D} = 13.9P_0$ and $t_{S1} = 16.5P_0$; *right-most images*: $t_{Q04D} = 15.5P_0$ and $t_{S1} = 18.0P_0$. The bottom two images have been extracted from our video08; a movie showing the development of the structures displayed in the top two images has been published in MFTD07.

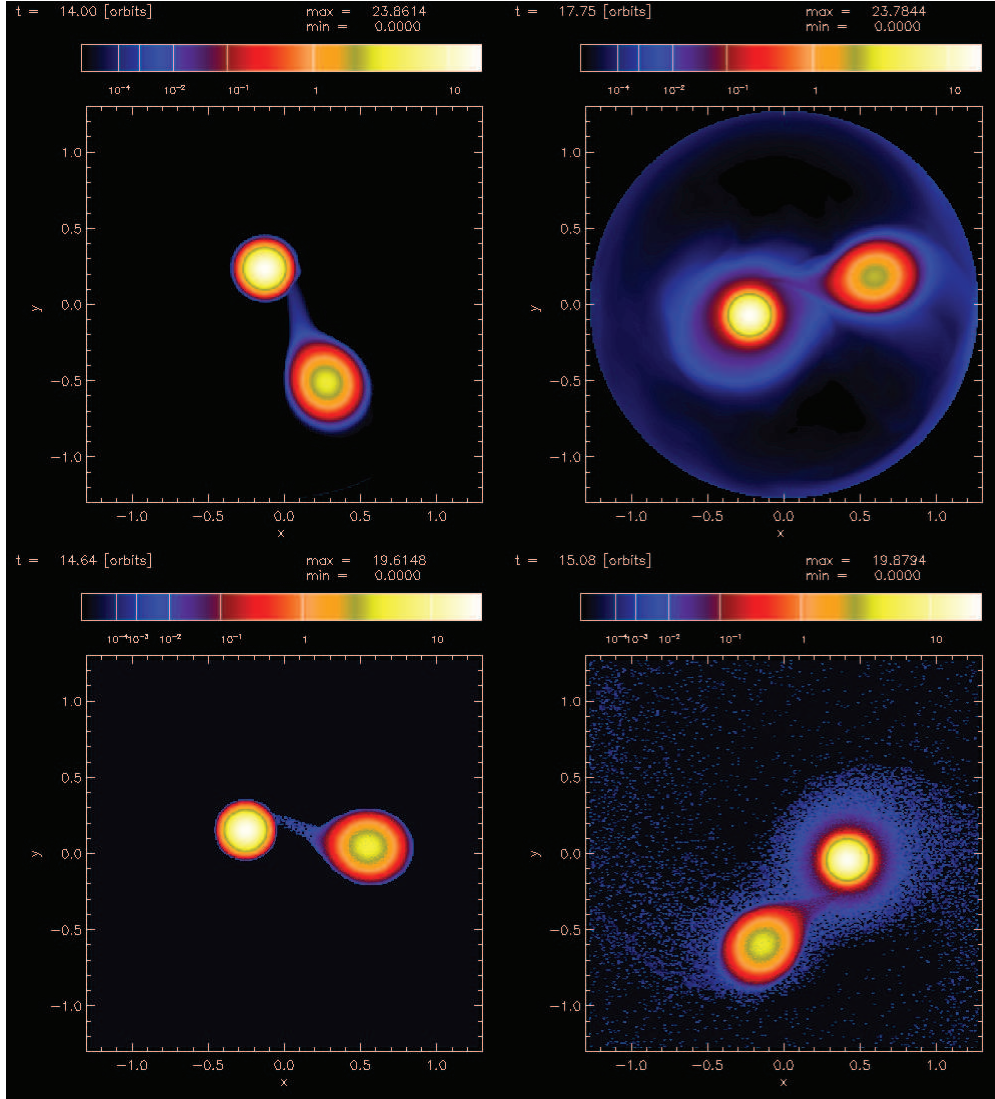


Fig. 9.— The images presented exemplify the qualitative difference between polytropic and ideal gas simulations. A hot tenuous envelope develops around one or both stars due to shock heating in the ideal gas simulations. Four selected frames from four simulations starting with initial model Q0.5 are shown: top row grid results, bottom row SPH results, left column polytropic simulations, right column ideal gas simulations. Since t_{zpt} is undefined in this case, the four frames were selected by eye to represent a similar stage in their time evolution.

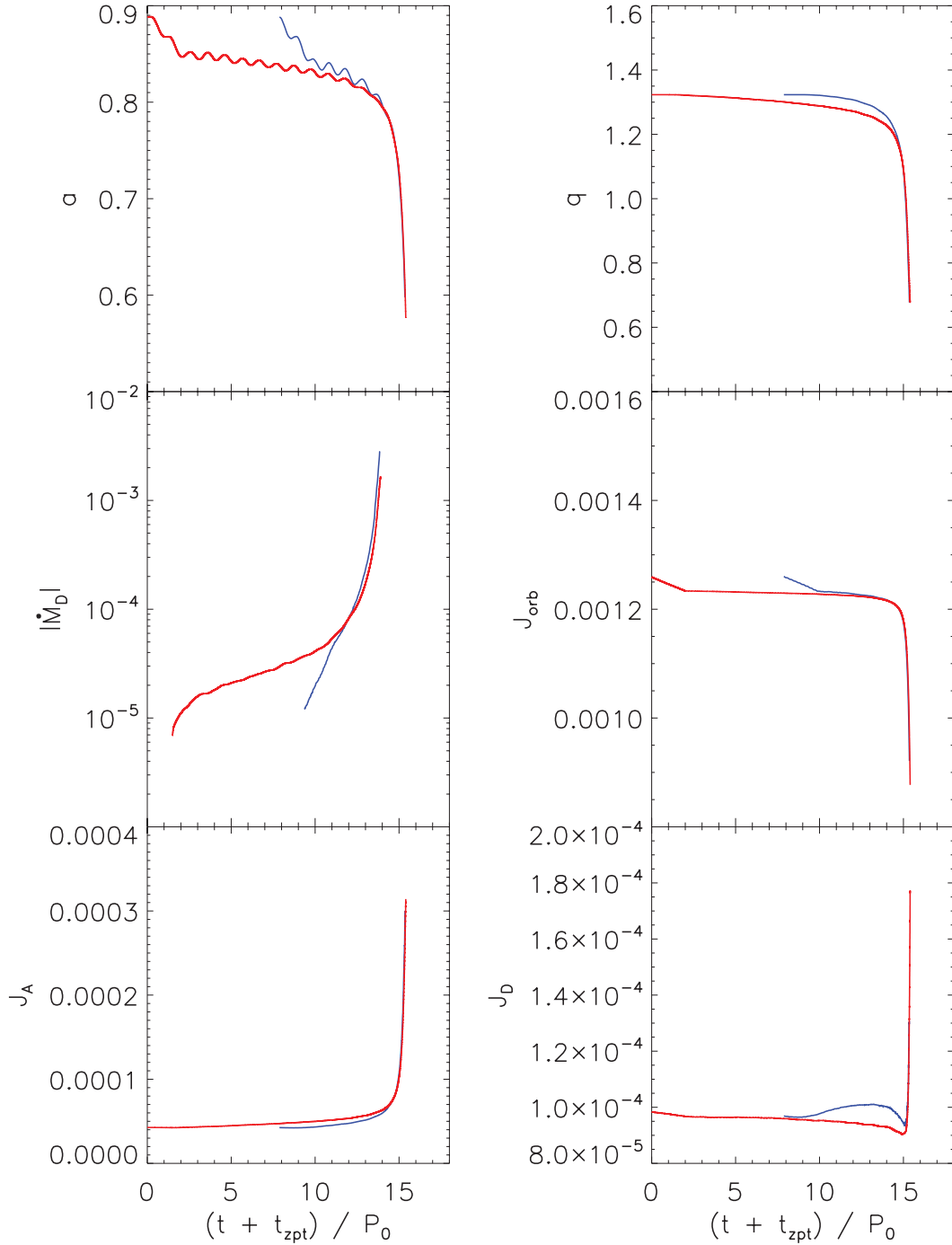


Fig. 10a.— Simulation Q1.3I. Curves show the time-dependent behavior of six system parameters as derived from models Q1.3I.G1 (solid red curves) and Q1.3I.S1 (solid blue curves). As detailed in Table 3, the SPH-code simulation includes a zero-point shift in time of $t_{zpt} = 7.85$.

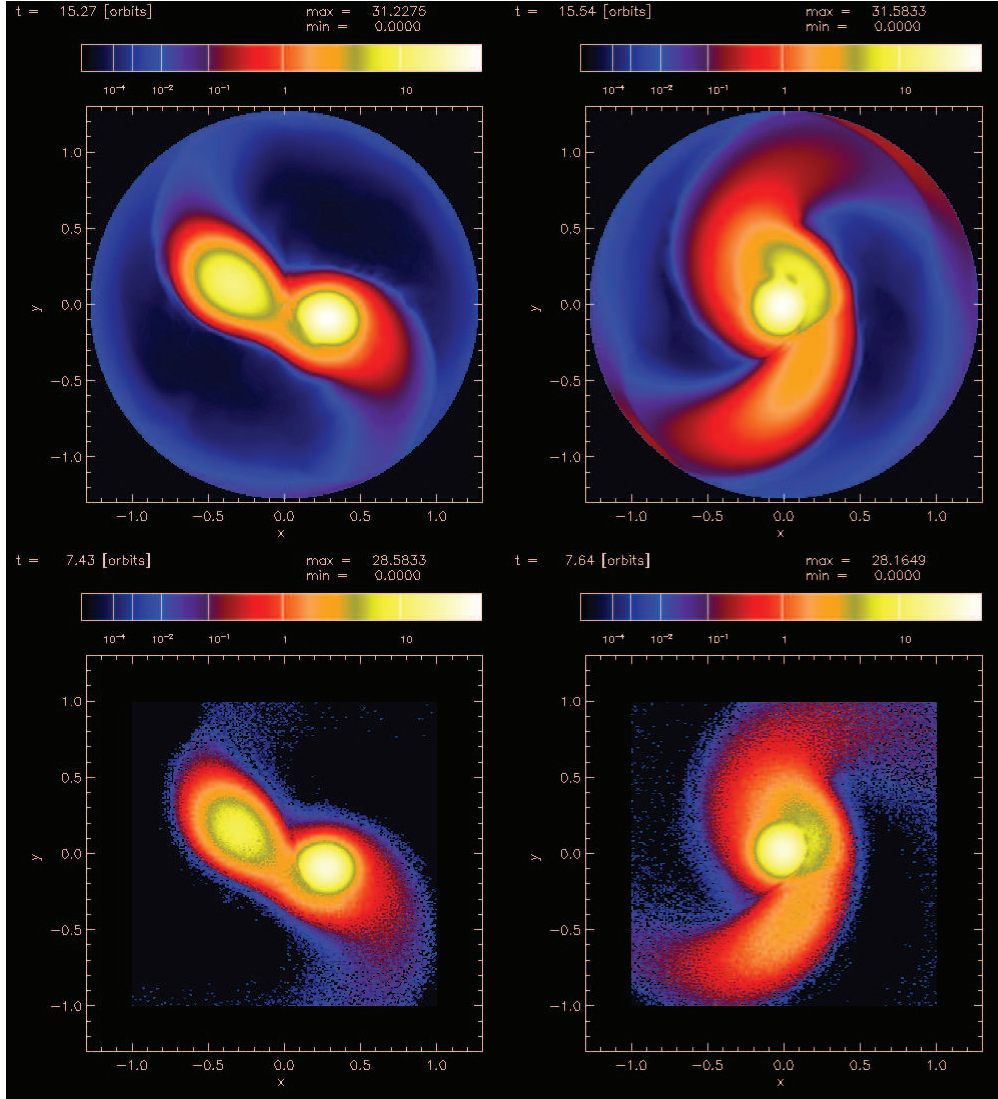


Fig. 10b.— Simulation Q1.3I. Images show contours of equatorial-plane column densities from model Q1.3I.G1 (top) and model Q1.3I.S1 (bottom) at two different points in time as the binary merger is occurring — specifically, *left-most images*: $t_{G1} = 15.27P_0$ and $t_{S1} = 7.43P_0$; *right-most images*: $t_{G1} = 15.54P_0$ and $t_{S1} = 7.64P_0$.

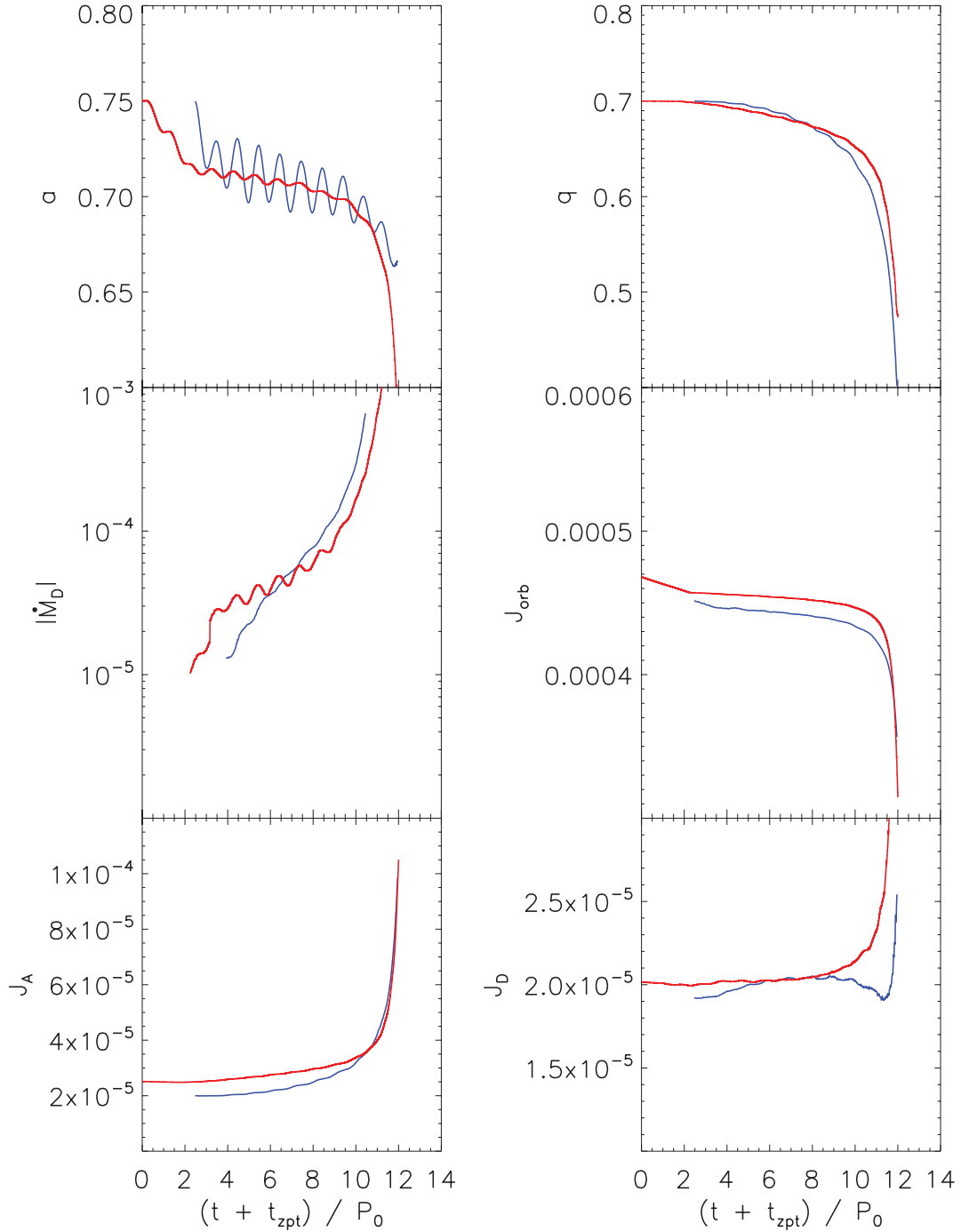


Fig. 11a.— Simulation Q0.7L. Curves show the time-dependent behavior of six system parameters as derived from models Q0.7L.G1 (solid red curves) and Q0.7L.S1 (solid blue curves). As detailed in Table 3, the SPH-code simulation includes a zero-point shift in time of $t_{zpt} = -8.7$.

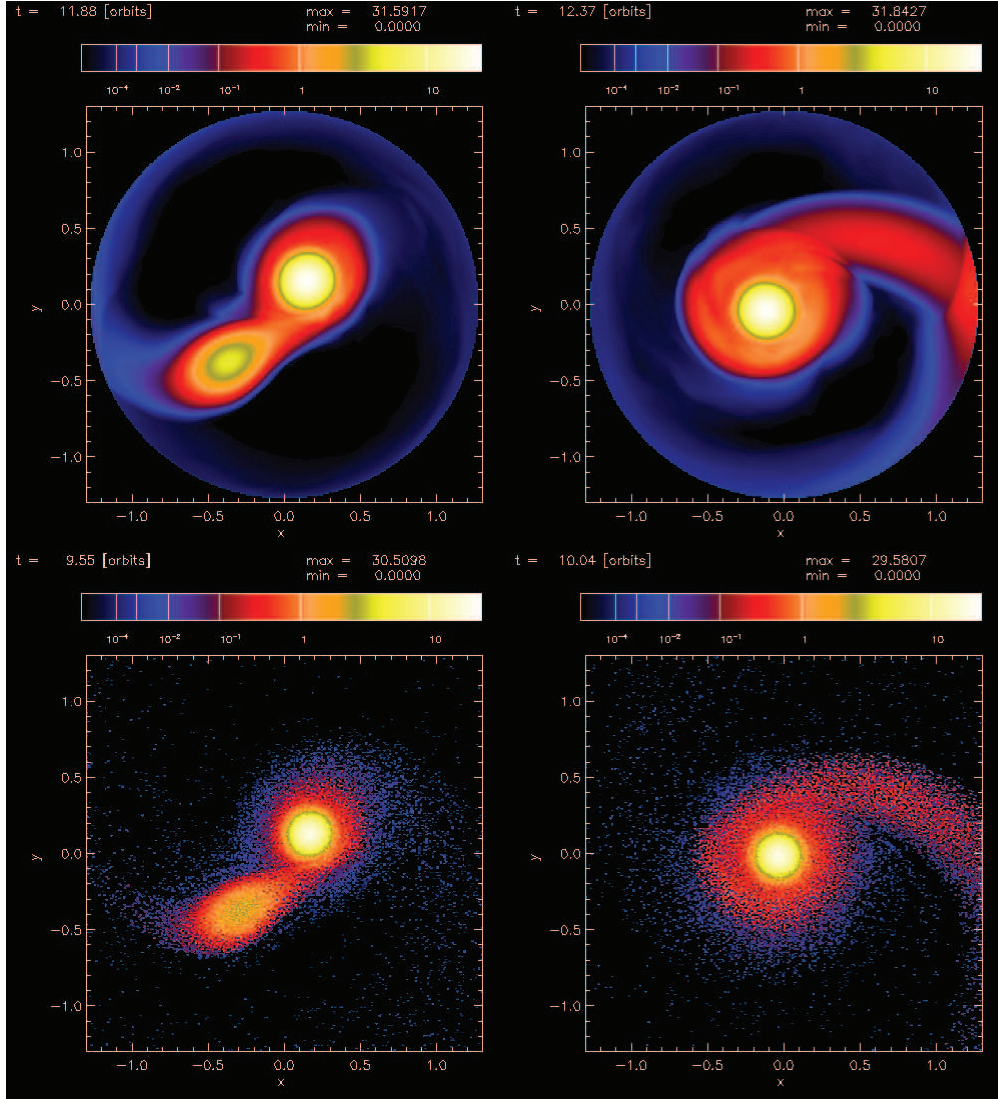


Fig. 11b.— Simulation Q0.7I. Images show contours of equatorial-plane column densities from model Q0.7LG1 (top) and model Q0.7LS1 (bottom) at two different points in time as the tidal destruction of the donor star is occurring — specifically, *left-most images*: $t_{G1} = 11.88P_0$ and $t_{S1} = 9.55P_0$; *right-most images*: $t_{G1} = 12.37P_0$ and $t_{S1} = 10.04P_0$.

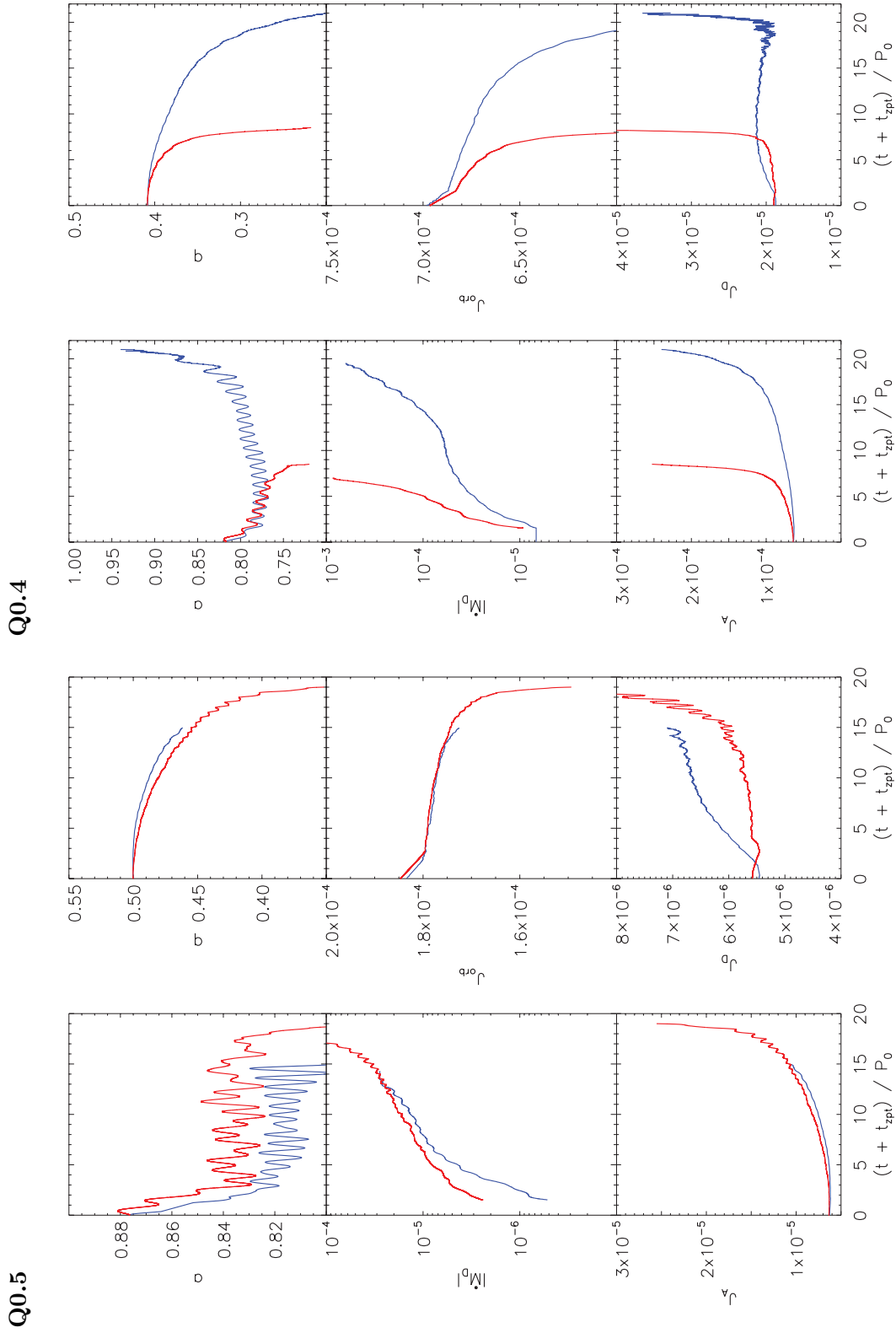


Fig. 12.— Simulations Q0.5I and Q0.4I. Same as Figure 5 except for ideal-gas equation of state. Left Panel: Results derived from models Q0.5L_G1 (red curves) and Q0.5L_S1 (blue curves). Right Panel: Results derived from models Q0.4L_G1 (red curves) and Q0.4L_S1 (blue curves).

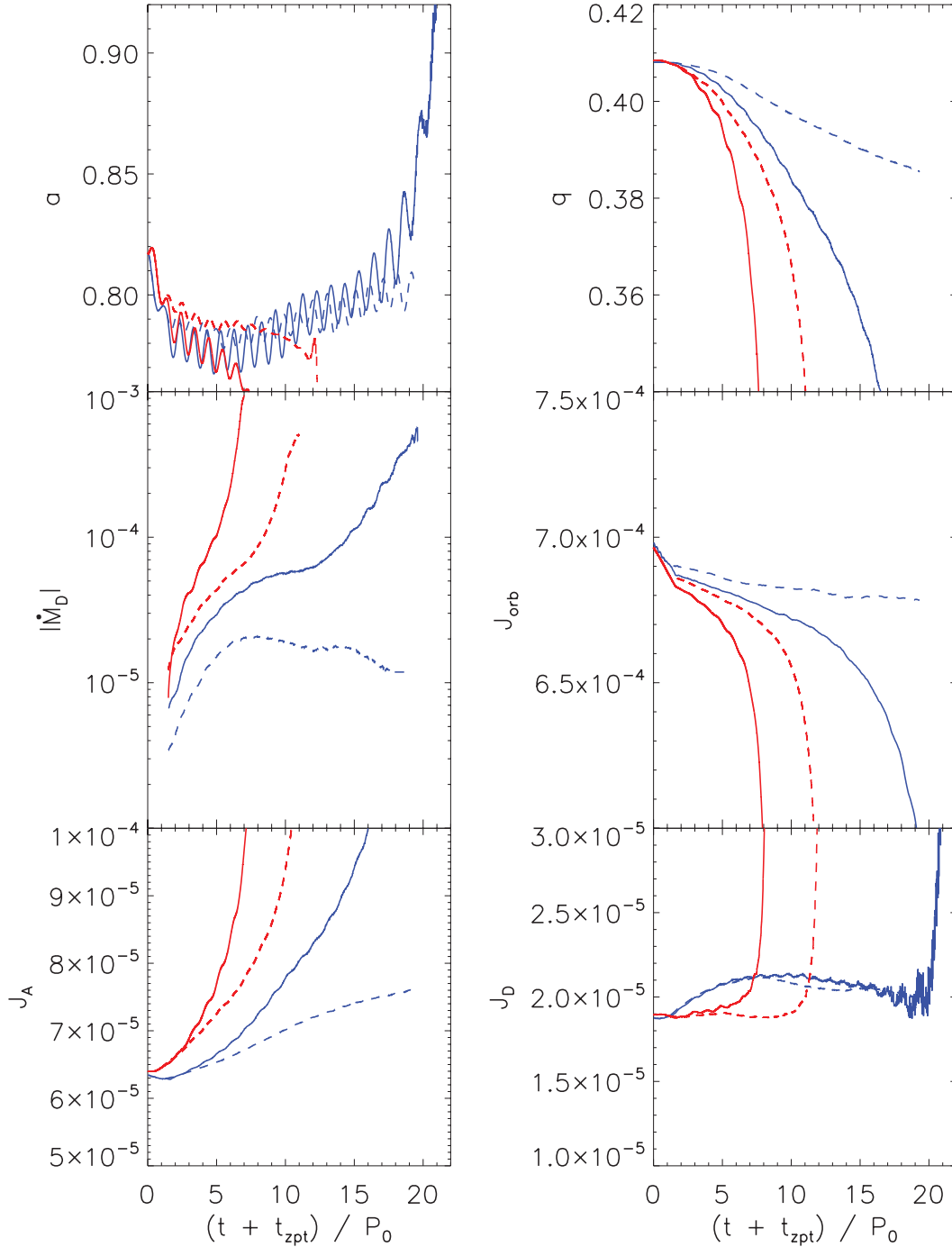


Fig. 13.— As in Figure 7, curves show the time-dependent behavior of six binary system parameters from model simulations Q0.4I. Blue curves are derived from SPH-code simulations and red curves are derived from grid-code simulations. Solid curves exactly reproduce information provided in the right panel of Figure 12 from simulations that were driven into contact for $1.6P_0$; for comparison, dashed curves present results from simulations Q0.4I_G2 and Q0.4I_S2 that were driven into contact for only $1.16P_0$.

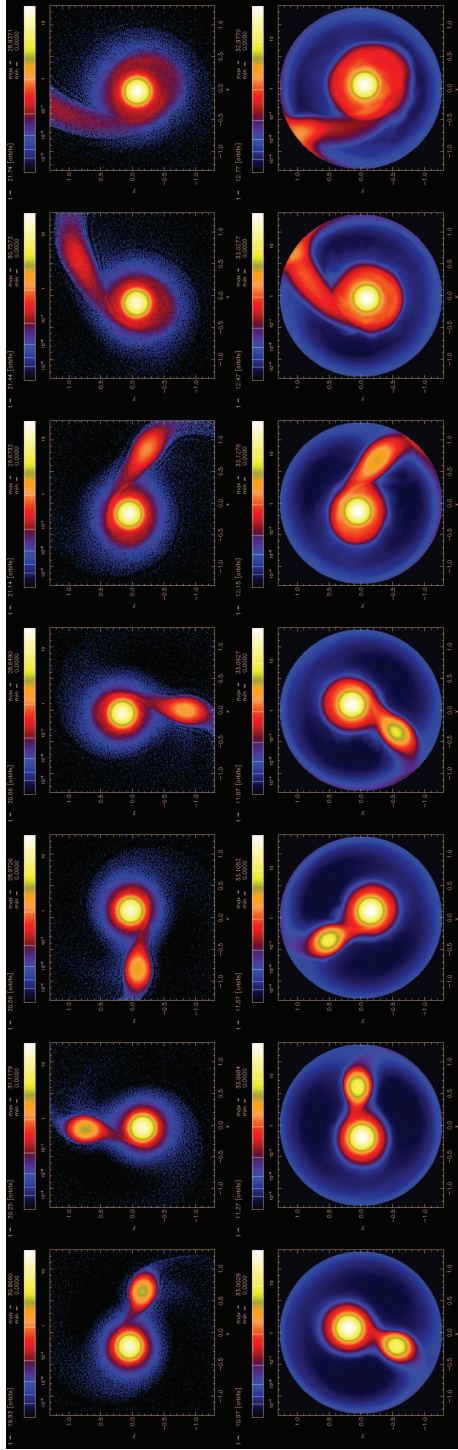


Fig. 14.— Seven images extracted from video19 and video21 that illustrate Q0.4I_S1 over the time period $19.93 \leq t/P_0 \leq 21.74$ and (bottom row) simulation Q0.4I_G1 over the time period $10.97 \leq t/P_0 \leq 12.77$, during the episode of tidal disruption of the donor. In both cases, adjacent images are separated in time by approximately $0.3P_0$ and the image sequence covers a total of $1.8P_0$.